Cryo-EM structure of a eukaryotic zinc transporter at a low pH suggests its Zn^{2+}-releasing mechanism

Senfeng Zhang[1,#], Chunting Fu[1,#], Yongbo Luo[2,#], Qingrong Xie[1], Tong Xu[1], Ziyi Sun[1,*], Zhaoming Su[2,*], Xiaoming Zhou[1,*]

[1]Department of Integrated Traditional Chinese and Western Medicine, Rare Diseases Center, State Key Laboratory of Biotherapy, West China Hospital, Sichuan University, Chengdu, Sichuan 610041, China

[2]The State Key Laboratory of Biotherapy, Department of Geriatrics and National Clinical Research Center for Geriatrics, West China Hospital, Sichuan University, Chengdu, Sichuan 610041, China

[#]These authors contributed equally to this work.

*To whom correspondence should be addressed:
Ziyi Sun, PhD, 17 Renmin Road South 3rd Section, Sichuan University, Chengdu, Sichuan 610041, China; Phone: +86 (28) 8540 1152; Email: ziyi.sun@scu.edu.cn
Zhaoming Su, PhD, 17 Renmin Road South 3rd Section, Sichuan University, Chengdu, Sichuan 610041, China; Phone: +86 (28) 8540 5028; Email: zsu@scu.edu.cn
Xiaoming Zhou, PhD, 17 Renmin Road South 3rd Section, Sichuan University, Chengdu, Sichuan 610041, China; Phone: +86 (28) 8540 1152; Email: x.zhou@scu.edu.cn

Keywords

ZnT8; SLC30; CDF; Protonation; Cryo-EM structure; Single-particle reconstruction; Membrane protein; Transport cycle; Conformational change

Abbreviations

Cryo-EM, cryo-electron microscopy; ZnT8, zinc transporter 8; SLC, solute carrier; TMD, transmembrane domain; CTD, carboxy-terminal domain; RMSD, root mean square deviation

Abstract

Zinc transporter 8 (ZnT8) is mainly expressed in pancreatic islet β cells and is responsible for H^+-coupled uptake (antiport) of Zn^{2+} into the lumen of insulin secretory granules. Structures of human ZnT8 and its prokaryotic homolog YiiP have provided structural basis for constructing a plausible transport cycle for Zn^{2+}. However, the mechanistic role that protons play in the transport process remains unclear. Here we present a lumen-facing cryo-EM structure of ZnT8 from *Xenopus tropicalis* (xtZnT8) in the presence of Zn^{2+} at a luminal pH (5.5). Compared to a Zn^{2+}-bound xtZnT8 structure at a cytosolic pH (7.5), the low-pH structure displays an empty transmembrane Zn^{2+}-binding site with a disrupted coordination geometry. Combined with a Zn^{2+}-binding assay our data suggest that protons may disrupt Zn^{2+} coordination at the transmembrane Zn^{2+}-binding site in the lumen-facing state, thus facilitating Zn^{2+} release from ZnT8 into the lumen.

Introduction

Zinc is the second most abundant trace metal in cells and plays critical roles in many biological processes, including cell growth and development, functioning of the central nervous system and the immune system (Kambe et al., 2015; Maret, 2013; Vallee and Falchuk, 1993). A variety of enzymes also require Zn^{2+} for their biological functions (Kambe et al., 2015; Maret, 2013; Vallee and Falchuk, 1993). Meanwhile, excessive cytoplasmic free Zn^{2+} is highly toxic. Therefore, the intracellular homeostasis of Zn^{2+} is tightly controlled, mainly by two classes of solute carrier (SLC) transporters: the ZRT/IRT-like proteins (ZIPs, or SLC39), and the cation-diffusion facilitators (CDFs, or SLC30), also known as zinc transporters (ZnTs) (Bin et al., 2018; Eide, 2006; Kambe et al., 2015). These two transporter families mediate influx and efflux of Zn^{2+} into and out of the cytoplasm of the cell, respectively. Among ZnTs, ZnT8 is mainly expressed in pancreatic islet β cells and is responsible for H^+-coupled uptake/antiport of Zn^{2+} into the lumen of insulin secretory granules, in which Zn^{2+} is complexed with insulin in a crystalline form and is co-secreted with insulin (Davidson et al., 2014). ZnT8 is often targeted by autoantibodies in type 1 diabetes (Kawasaki, 2012; Wenzlau et al., 2007), whereas mutations and single nucleotide polymorphisms of ZnT8 are associated with type 2 diabetes (Flannick et al., 2014; Saxena et al., 2007; Scott et al., 2007; Sladek et al., 2007; Zeggini et al., 2007).

High-resolution structures of the ZnT family were first obtained with its prokaryotic homolog, YiiP from *Escherichia coli* (ecYiiP) (Lu and Fu, 2007; Lu et al., 2009) or *Shewanella oneidensis* (soYiiP) (Coudray et al., 2013; Lopez-Redondo et al., 2021; Lopez-Redondo et al., 2018), revealing a homodimeric configuration of YiiP. Recently, structures of human ZnT8 (hZnT8) were determined by single-particle cryo-electron microscopy (cryo-EM) (Xue et al., 2020), also as a homodimer (Fig. 1A). Four Zn^{2+}-binding sites were identified in each hZnT8 protomer (Xue et al., 2020): one S_{TMD} site at the center of the transmembrane domain (TMD), two adjacent S_{CTD} sites in the carboxy-terminal domain (CTD), and one $S_{interface}$ site at the interface between TMD and CTD (Fig. 1A). S_{TMD} is the primary site for Zn^{2+} binding and transport, whereas the S_{CTD} sites are formed by residues from both protomers and contribute to hZnT8 dimerization (Xue et al., 2020). These three Zn^{2+}-binding sites are highly conserved in the ZnT family (Fig. 2), including the prokaryotic YiiP (Lopez-Redondo et al., 2018; Lu and Fu, 2007). On the other hand,

the $S_{interface}$ site seems less conserved. In hZnT8, it is formed by residues from both CTD and a loop region between TM2 and TM3 (Xue et al., 2020), while in YiiP it is formed solely by residues from the TM2-TM3 loop (Lopez-Redondo et al., 2018; Lu and Fu, 2007). In some species like mice and rats, no Zn^{2+}-coordinating residue (Cys, His, Glu or Asp) is present within the predicted TM2-TM3 loop (Fig. 2), further suggesting that $S_{interface}$ may not be conserved. Nonetheless, it has been hypothesized that $S_{interface}$ may increase the local concentration of Zn^{2+} to facilitate its binding to the S_{TMD} site in ZnT8 (Xue et al., 2020).

The structures of hZnT8 and YiiP were captured in both outward-facing (lumen-facing) and inward-facing (cytosol-facing) states (Lopez-Redondo et al., 2018; Lu and Fu, 2007; Xue et al., 2020), allowing construction of an alternating-access model for ZnT8 transporters as follows (Fig. 1B). (1) Due to a slightly basic cytosolic pH (Llopis et al., 1998; Stiernet et al., 2007), a counter-transported H^+ is released to the cytosol from ZnT8 in the cytosol-facing state, allowing a cytosolic Zn^{2+} to bind to the S_{TMD} site. (2) ZnT8 transits to the lumen-facing state. (3) The S_{TMD}-bound Zn^{2+} is released to the granule lumen while the acidic luminal pH (Hutton, 1982) protonates the S_{TMD} site of ZnT8. (4) ZnT8 transits back to the cytosol-facing state, ready for the next cycle. The model is consistent with the structural and functional data reported for ZnTs regarding H^+-coupled Zn^{2+} binding and transport (Ohana et al., 2009; Shusterman et al., 2014; Xue et al., 2020). However, the role of H^+ binding in this process (i.e. step 3) remains speculative.

In this study, we compared two lumen-facing cryo-EM structures of ZnT8 from *Xenopus tropicalis* (xtZnT8) in the presence of Zn^{2+} at either a cytosolic pH (7.5) or a luminal pH (5.5) to assess the effect of H^+ binding on ZnT8 in the lumen-facing state. Together with a Zn^{2+}-binding analysis our data suggest a role of protons that may facilitate the release of Zn^{2+} from ZnT8 into the lumen.

Results

Cryo-EM structure of xtZnT8 with Zn^{2+} at a cytosolic pH (7.5) in a lumen-facing state

First, we determined the structure of xtZnT8 in the presence of 1 mM Zn^{2+} at a cytosolic pH of 7.5 (3.9 Å, xtZnT8-Zn^{2+}) by cryo-EM (Fig. 3). XtZnT8 shares 58% sequence identity and 83%

sequence similarity to hZnT8 (Fig. 2). Similar to the Zn^{2+}-bound hZnT8 structure (hZnT8-Zn^{2+}, PDB: 6XPE), the xtZnT8-Zn^{2+} structure is also organized as a homodimer (Fig. 4A). Structural alignment between individual protomers of xtZnT8-Zn^{2+} and hZnT8-Zn^{2+} yielded a root mean square deviation (RMSD) of 1.18 Å with all C_α atoms aligned, while the major deviation came from flexible loop regions of the two proteins, indicating that the two structures are highly alike (Fig. 4A). Similarly, each protomer of xtZnT8-Zn^{2+} has two adjacent S_{CTD} sites (S_{CTD1} and S_{CTD2}), which are formed by the HCH (His45-Cys46-His47) motif from one protomer and multiple Zn^{2+}-coordinating residues from the other protomer, occupied by two Zn^{2+} (Fig. 2 and 4B). Also, the xtZnT8-Zn^{2+} structure has one Zn^{2+} bound at the S_{TMD} site with a tetrahedral coordination, which is formed by His100 and Asp104 from TM2, and His225 and Asp229 from TM5 (Fig. 2 and 4C). Consistently, the S_{TMD} residues are highly conserved in eukaryotic species with the 2-His-2-Asp configuration (Cotrim et al., 2019; Hoch et al., 2012) (Fig. 2). Like the hZnT8-Zn^{2+} structure, the S_{TMD}-bound Zn^{2+} in xtZnT8-Zn^{2+} is accessible by solvent from the luminal side (Fig. 4D), indicating that the transporter is lumen-facing. Therefore, the xtZnT8-Zn^{2+} structure was also captured in a Zn^{2+}-bound lumen-facing state similar to hZnT8-Zn^{2+} (Xue et al., 2020). Interestingly, the S_{TMD}-bound Zn^{2+} was not released automatically from the S_{TMD} site in the lumen-facing state, suggesting that a Zn^{2+}-releasing mechanism is required for eukaryotic ZnT8.

A lumen-facing cryo-EM structure of xtZnT8 at a luminal pH (5.5)

It has been assumed that binding of luminal protons to the S_{TMD} site (likely histidine residues) in a Zn^{2+}-bound lumen-facing ZnT8 would weaken Zn^{2+} binding and promote Zn^{2+} release to the lumen (Xue et al., 2020) due to an acidic pH (5~6) of insulin secretory granules (Hutton, 1982). Similar assumptions have been proposed for YiiPs as a Zn^{2+}-releasing mechanism (Gupta et al., 2014; Lopez-Redondo et al., 2018). However, structural evidence to support this hypothesis is lacking. To investigate the effect of protons on Zn^{2+} binding in ZnT8, we then determined another cryo-EM structure of xtZnT8 in the presence of 1 mM Zn^{2+} at a luminal pH of 5.5 (3.7 Å, xtZnT8-H^+) (Fig. 5). The xtZnT8-H^+ sample was prepared in the same way as the xtZnT8-Zn^{2+} sample except that the former underwent an additional buffer exchange step from pH 7.5 to pH

5.5. Ideally, this experimental design would allow us to assess the effect of protons when they bind to xtZnT8-Zn^{2+}.

Interestingly, the xtZnT8-H^+ structure also adopts a lumen-facing conformation, similar to xtZnT8-Zn^{2+} (Fig. 6A). Superposition of the two xtZnT8 structures yielded an all-atom RMSD of 0.58 Å, indicating that xtZnT8-H^+ and xtZnT8-Zn^{2+} are very alike (Fig. 6A). However, one prominent difference between the two structures is that the side chain of His100 in xtZnT8-H^+ is pointing toward the luminal side, thus disrupting the tetrahedral coordination for Zn^{2+} at the S_{TMD} site (Fig. 6B). Consistently, no Zn^{2+} density was observed at S_{TMD} in xtZnT8-H^+ even in the presence of 1 mM Zn^{2+} (Fig. 6C). This data suggests that exposure of xtZnT8-Zn^{2+} to protons at a luminal pH causes release of the bound Zn^{2+} from the S_{TMD} site, providing structural evidence to support protonation as a Zn^{2+}-releasing mechanism in ZnT8.

Protons disrupt Zn^{2+} binding in xtZnT8

A functional inference from the xtZnT8-H^+ structure is that protons at a luminal pH (e.g. 5.5) would disrupt Zn^{2+} binding to xtZnT8. To test this idea, we used microscale thermophoresis (MST) (Jerabek-Willemsen et al., 2011) to measure Zn^{2+} binding to xtZnT8 in various conditions. First, we titrated Zn^{2+} to wild-type xtZnT8 purified in the absence of Zn^{2+} at a cytosolic pH of 7.5. The MST data was readily fit by an inverse S-shaped curve (Fig. 7A), with an equilibrium dissociation constant (K_d) of 4.91 ± 0.39 μM for Zn^{2+}. The titrated Zn^{2+} binding can be attributed to the S_{TMD} site of xtZnT8, as an S_{TMD}-double-mutant (H100A/H225A) showed a noise-like trendless no-binding pattern when Zn^{2+} was titrated (Fig. 7B). We then titrated Zn^{2+} to wild-type xtZnT8 purified in the absence of Zn^{2+} at a luminal pH of 5.5 and obtained a noise-like no-binding pattern as well (Fig. 7C), suggesting that protons at a low pH disrupt Zn^{2+} binding to the S_{TMD} site of xtZnT8. These data are consistent with the xtZnT8 structures.

Discussion

A potential Zn^{2+}-releasing mechanism in ZnT8

Another major difference between the two xtZnT8 structures is that a portion of TM2 (Ala93-Ala98), which is close to the luminal side, appears more flexible in xtZnT8-Zn^{2+} than in xtZnT8-H^+, and therefore is less visible in the former map (Fig. 8A). This is reminiscent of hZnT8-Zn^{2+} (PDB: 6XPE) and the structure of its S_{TMD}-double-mutant (hZnT8-D110N/D224N, PDB: 6XPD), which mimics a protonated state at positions 110 and 224 and doesn't bind Zn^{2+} at the mutated S_{TMD} site (Xue et al., 2020). Compared to hZnT8-D110N/D224N, the hZnT8-Zn^{2+} structure also shows a less defined TM2 portion near the luminal side (Fig. 8B). This result suggests that in the lumen-facing state of ZnT8, binding of Zn^{2+} at S_{TMD} may increase the flexibility of the near-lumen TM2 region, thus allowing or increasing solvent access from the luminal side. Therefore, a potential Zn^{2+}-releasing mechanism for ZnT8 can be proposed as in Fig. 8C. Briefly, in the Zn^{2+}-bound lumen-facing state of xtZnT8, the TM2 region near the luminal side becomes flexible, allowing luminal protons (pH 5~6) to access and protonate the S_{TMD} site (likely His100/His225), which disrupts Zn^{2+} coordination and facilitates Zn^{2+} release from S_{TMD} to the lumen.

Other features of the xtZnT8-Zn^{2+} structure compared to hZnT8-Zn^{2+}

Meanwhile, structural comparison between xtZnT8-Zn^{2+} and hZnT8-Zn^{2+} reveals two apparent differences. First, no Zn^{2+} density was observed in the $S_{interface}$ site in xtZnT8-Zn^{2+} (His131/His350) even in the presence of 1 mM Zn^{2+} (Fig. 9A), while the $S_{interface}$ Zn^{2+} has been clearly observed between His137 and His345 in hZnT8-Zn^{2+} (Xue et al., 2020). This difference could be due to different experimental procedures or maybe reflect a less conservation of $S_{interface}$ among ZnT8 species (Fig. 2). Second, the region between the HCH motif and TM1 (HCH-TM1-linker) assumed an α helical structure as a continuation of the TM1 helix in xtZnT8-Zn^{2+}. In hZnT8-Zn^{2+}, HCH-TM1-linker was not resolved (Fig. 9B), suggesting that this region may adopt a flexible/unordered conformation. It is noteworthy that the distance between the HCH motif and TM1 varies substantially (> 10 Å) between different hZnT8 conformations (Xue et al., 2020), mandating that HCH-TM1-linker is capable of changing conformations. Therefore, the different conformations of HCH-TM1-linker could be a mechanism for regulating conformational changes in eukaryotic ZnT8 (Xue et al., 2020). Further studies will be required to address this question.

Materials and methods

Protein expression and purification

The gene encoding the full-length wild-type ZnT8 from *Xenopus tropicalis* (xtZnT8, NCBI accession: NP_001011041.1) was synthesized by Genewiz (Suzhou, China) in a modified pPICZ plasmid (Thermo Fisher Scientific) containing a carboxy-terminal tag of Tobacco etch virus (TEV) protease recognition site and decahistidine. The bacterial cytochrome b562RIL (BRIL) (Chu et al., 2002) was fused to the carboxy-end of the xtZnT8 protein before the TEV site. Mutations were introduced by site-directed mutagenesis using QuikChange II system (Agilent, Santa Clara, CA) according to manufacturer's recommendation, and all mutations were verified by sequencing. The xtZnT8-BRIL fusion protein (referred to as xtZnT8 in this study) was overexpressed in yeast (*Pichia pastoris* strain GS115) cells by adding 1% (v/v) methanol and 2.5% (v/v) dimethyl sulfoxide (DMSO) at $OD_{600\,nm}$ of ~1 and shaking at 20 °C for 48 h. Cell pellets were resuspended in lysis solution (LS) containing 20 mM Tris-HCl pH 7.5, 150 mM NaCl, 10% (v/v) glycerol, 1 mM phenylmethanesulfonyl fluoride (PMSF) and 2 mM β-mercaptoethanol, and were lysed by an ATS AH-1500 high-pressure homogenizer (Shanghai, China) at 1,300 MPa. Protein was extracted by addition of 1% (w/v) n-dodecyl-β-D-maltopyranoside (DDM, Anatrace) and 0.1% (w/v) cholesteryl hemisuccinate (CHS, Anatrace) at 4 °C for 2 h and the extraction mixture was centrifuged at 200,000 x g for 20 min at 4 °C. The supernatant was then loaded onto a cobalt metal affinity column, washed with 20 bed-volume of LS containing 1 mM DDM, 0.01% (w/v) CHS and 40 mM imidazole pH 8.0, and eluted with LS supplemented with 1 mM DDM, 0.01% (w/v) CHS and 250 mM imidazole pH 8.0.

Cryo-EM sample preparation and image acquisition

Affinity-purified xtZnT8 was concentrated to 6-8 mg/ml and loaded onto a Superdex 200 Increase 10/300 GL column (GE Healthcare), and was further purified by size-exclusion chromatography (SEC). For xtZnT8-Zn^{2+}, the SEC buffer contained 20 mM Tris-HCl pH 7.5, 150 mM NaCl, 5 mM β-mercaptoethanol, 0.5 mM DDM and 1 mM $ZnSO_4$. For xtZnT8-H^+, SEC-

purified xtZnT8-Zn^{2+} underwent an additional SEC purification in 20 mM MES-Na pH 5.5, 150 mM NaCl, 5 mM β-mercaptoethanol, 0.5 mM DDM and 1 mM $ZnSO_4$. Freshly SEC-purified xtZnT8 was then concentrated to 8 mg/ml as approximated by ultraviolet absorbance, and 3 µl of the protein solution was applied to glow-discharged (45 s) Quantifoil R2/1 300-mesh gold grids (Quantifoil Micro Tools GmbH, Germany). The grids were blotted with standard Vitrobot filter paper for 2.5 s at 4 °C under 100% humidity and plunged into liquid ethane using a Vitrobot Mark IV (Thermo Fisher Scientific). The frozen grids were loaded into a Titan Krios electron microscope (Thermo Fisher Scientific) operated at 300 kV with the condenser lens aperture at 50 µm. Microscope magnification was at 130,000× (1.1 Å per pixel) for xtZnT8-Zn^{2+} and 165,000× (0.85 Å per pixel) for xtZnT8-H^+. Movie stacks were collected automatically using the EPU software (Version 2.9.0.1519REL, Thermo Fisher Scientific) on a K2 Summit direct electron camera (Gatan) equipped with a Quantum GIF energy filter with an energy slit of 20 eV in counting mode. Data were collected at 5 raw frames per second for 6 s, yielding 30 frames per stack and a total exposure dose of 50.1 $e^-/Å^2$ for xtZnT8-Zn^{2+} and 63.9 $e^-/Å^2$ for xtZnT8-H^+. A total of 2,961 movie stacks for xtZnT8-Zn^{2+} and 2,258 movie stacks for xtZnT8-H^+ were collected at a defocus range of -1.0 to -1.7 µm.

Cryo-EM data processing and 3D reconstruction

The movie stacks of xtZnT8-Zn^{2+} were motion-corrected and dose-weighted using the MotionCor2 program (Zheng et al., 2017). CTF correction was performed using the Gctf program (Zhang, 2016). The rest of the data processing was carried out in RELION 3.1 (Zivanov et al., 2018) except the last step. About 20 micrographs from the xtZnT8-Zn^{2+} dataset were used for manual picking of ~1000 particles, which were used for an initial 2D classification. Class averages representing projections of the xtZnT8 dimer in different orientations were selected as templates for automated particle picking from the full dataset. A total of 928,822 particles were picked from 2,943 micrographs. Particles extracted from the dataset were binned by a factor of 3 and subjected to reference-free 2D classification, and particles in good 2D classes were selected (518,886 good particles in total). Using a subset of the selected good particles a

coarse initial 3D model was generated first, followed by a one-class (K=1) global 3D classification with all good particles to generate a fine initial 3D model. Using the fine initial 3D model, all good particles were subjected to a four-class (K=4) local 3D classification with an angular search step of 3.75°. The local 3D classification step was performed in six parallel runs, and particles of the best 3D class from each run were combined and duplicate particles were removed, resulting in 380,810 particles. The re-extracted unbinned particles were then subjected to a final six-class multi-reference 3D classification using the best 3D classes from the local 3D classification step as references. The resulting best 3D class containing 233,408 particles was subjected to per-particle defocus refinement, beam-tilt refinement and Bayesian polishing, and was subsequently imported into CryoSPARC 3.2 (Punjani et al., 2017). After Non-uniform refinement (Punjani et al., 2020) in CryoSPARC, the final reconstruction was solved at an overall resolution of 3.9 Å. For the xtZnT8-H^+ dataset, a total of 684,578 particles were picked from 2,230 micrographs. The same image processing procedure was utilized except that a low-pass-filtered map of xtZnT8-Zn^{2+} was used as the initial model for the xtZnT8-H^+ particles. Eventually, 101,706 particles were selected from the best 3D class, yielding a 3D reconstruction map at 3.7 Å resolution.

Model building and refinement

Density maps of xtZnT8-Zn^{2+} and xtZnT8-H^+ were of sufficient quality for de novo model building in Coot (Emsley and Cowtan, 2004), facilitated by a published structure of hZnT8 (PDB: 6XPE). The xtZnT8 models were manually adjusted and rebuilt in Coot and refined using the phenix.real_space_refine module (Afonine et al., 2018) in PHENIX (Adams et al., 2010). Model geometries were assessed by Molprobity (Davis et al., 2007) and summarized in Table 1. Structural figures were generated using PyMOL (Schrödinger, LLC) and UCSF Chimera (Pettersen et al., 2004). Accessibility analysis was performed using the volume-filling program HOLLOW (Ho and Gruswitz, 2008) with default settings.

Microscale thermophoresis (MST)

MST analysis was performed using Monolith NT.115 (NanoTemper Technologies, Germany) by staining His-tagged xtZnT8 with the RED-Tris-NTA 2nd Generation dye (NanoTemper Technologies, Germany). For Zn^{2+} titration, affinity-purified xtZnT8 was further purified by SEC in a buffer containing 150 mM NaCl, 1 mM DDM, and either 20 mM HEPES-Na pH 7.5 or 20 mM MES-Na pH 5.5 as designed. Peak fractions were pooled and diluted to 200 nM using the SEC buffer, and mixed with 100 nM RED-Tris-NTA 2nd Generation dye at a 1:1 ratio and incubated for 30 min at room temperature. Then the sample was centrifuged at 15,000 x g for 10 min at 4 °C to keep the supernatant containing the labeled protein. Freshly-prepared serial-diluted $ZnSO_4$ solutions were used as the titrant and were prepared according to the MST manual with 1 mM as the highest concentration used. The labeled protein was mixed with serial-diluted Zn^{2+} and incubated for 30 min at room temperature. Then the protein sample series were loaded into capillaries and MST measurements were performed according to the Monolith manual. The equilibrium dissociation constant (K_d) was determined using the MO.Affinity Analysis software (NanoTemper Technologies, Germany) with the K_d fit function, and a noise-like trendless pattern for all data points in a measurement that fails the K_d fit function was deemed a no-binding pattern. All MST measurements were performed in three independently repeated experiments, and K_d was expressed as mean ± standard deviation (SD) in the text.

Data Availability

The cryo-EM density maps for xtZnT8-Zn^{2+} and xtZnT8-H^{+} have been deposited in the Electron Microscopy Data Bank under the accession IDs EMD-33619 and EMD-33620, respectively. The atomic coordinates of the xtZnT8-Zn^{2+} and xtZnT8-H^{+} structures have been deposited in the Protein Data Bank under the accession codes 7Y5G and 7Y5H, respectively. Two previously published hZnT8 structures used in this study are available in the Protein Data Bank under accession codes 6XPD and 6XPE.

Acknowledgements

Cryo-EM data were collected at SKLB West China Cryo-EM Center and were processed at the Duyu High Performance Computing Center of Sichuan University.

Funding and additional information

This work was supported in part by the National Natural Science Foundation of China (NSFC) grant 31770783 to Xiaoming Zhou and 32070049 to Zhaoming Su, the 1.3.5 Project for Disciplines of Excellence grant by West China Hospital of Sichuan University to Xiaoming Zhou and Zhaoming Su, and Ministry of Science and Technology of China grant 2021YFA1301900 to Zhaoming Su.

Conflict of interest

The authors declare that they have no conflicts of interest with the contents of this article.

References

Adams, P.D., Afonine, P.V., Bunkoczi, G., Chen, V.B., Davis, I.W., Echols, N., Headd, J.J., Hung, L.W., Kapral, G.J., Grosse-Kunstleve, R.W., McCoy, A.J., Moriarty, N.W., Oeffner, R., Read, R.J., Richardson, D.C., Richardson, J.S., Terwilliger, T.C., Zwart, P.H., 2010. PHENIX: a comprehensive Python-based system for macromolecular structure solution. Acta Crystallogr D Biol Crystallogr 66, 213-221.

Afonine, P.V., Poon, B.K., Read, R.J., Sobolev, O.V., Terwilliger, T.C., Urzhumtsev, A., Adams, P.D., 2018. Real-space refinement in PHENIX for cryo-EM and crystallography. Acta Crystallogr D Struct Biol 74, 531-544.

Bin, B.H., Seo, J., Kim, S.T., 2018. Function, Structure, and Transport Aspects of ZIP and ZnT Zinc Transporters in Immune Cells. J Immunol Res 2018, 9365747.

Chu, R., Takei, J., Knowlton, J.R., Andrykovitch, M., Pei, W., Kajava, A.V., Steinbach, P.J., Ji, X., Bai, Y., 2002. Redesign of a four-helix bundle protein by phage display coupled with proteolysis and structural characterization by NMR and X-ray crystallography. J Mol Biol 323, 253-262.

Combet, C., Blanchet, C., Geourjon, C., Deleage, G., 2000. NPS@: network protein sequence analysis. Trends Biochem Sci 25, 147-150.

Cotrim, C.A., Jarrott, R.J., Martin, J.L., Drew, D., 2019. A structural overview of the zinc transporters in the cation diffusion facilitator family. Acta Crystallogr D Struct Biol 75, 357-367.

Coudray, N., Valvo, S., Hu, M., Lasala, R., Kim, C., Vink, M., Zhou, M., Provasi, D., Filizola, M., Tao, J., Fang, J., Penczek, P.A., Ubarretxena-Belandia, I., Stokes, D.L., 2013. Inward-facing conformation of the zinc transporter YiiP revealed by cryoelectron microscopy. Proc Natl Acad Sci U S A 110, 2140-2145.

Davidson, H.W., Wenzlau, J.M., O'Brien, R.M., 2014. Zinc transporter 8 (ZnT8) and beta cell function. Trends Endocrinol Metab 25, 415-424.

Davis, I.W., Leaver-Fay, A., Chen, V.B., Block, J.N., Kapral, G.J., Wang, X., Murray, L.W., Arendall, W.B., 3rd, Snoeyink, J., Richardson, J.S., Richardson, D.C., 2007. MolProbity: all-atom contacts and structure validation for proteins and nucleic acids. Nucleic Acids Res 35, W375-383.

Eide, D.J., 2006. Zinc transporters and the cellular trafficking of zinc. Biochim Biophys Acta 1763, 711-722.

Emsley, P., Cowtan, K., 2004. Coot: model-building tools for molecular graphics. Acta Crystallogr D Biol Crystallogr 60, 2126-2132.

Flannick, J., Thorleifsson, G., Beer, N.L., Jacobs, S.B., Grarup, N., Burtt, N.P., Mahajan, A., Fuchsberger, C., Atzmon, G., Benediktsson, R., Blangero, J., Bowden, D.W., Brandslund, I., Brosnan, J., Burslem, F., Chambers, J., Cho, Y.S., Christensen, C., Douglas, D.A., Duggirala, R., Dymek, Z., Farjoun, Y., Fennell, T., Fontanillas, P., Forsen, T., Gabriel, S., Glaser, B., Gudbjartsson, D.F., Hanis, C., Hansen, T., Hreidarsson, A.B., Hveem, K., Ingelsson, E., Isomaa, B., Johansson, S., Jorgensen, T., Jorgensen, M.E., Kathiresan, S., Kong, A., Kooner, J., Kravic, J., Laakso, M., Lee, J.Y., Lind, L., Lindgren, C.M., Linneberg, A., Masson, G., Meitinger, T., Mohlke, K.L., Molven, A., Morris, A.P., Potluri, S., Rauramaa, R., Ribel-Madsen, R., Richard, A.M., Rolph, T., Salomaa, V., Segre, A.V., Skarstrand, H.,

Steinthorsdottir, V., Stringham, H.M., Sulem, P., Tai, E.S., Teo, Y.Y., Teslovich, T., Thorsteinsdottir, U., Trimmer, J.K., Tuomi, T., Tuomilehto, J., Vaziri-Sani, F., Voight, B.F., Wilson, J.G., Boehnke, M., McCarthy, M.I., Njolstad, P.R., Pedersen, O., Go, T.D.C., Consortium, T.D.G., Groop, L., Cox, D.R., Stefansson, K., Altshuler, D., 2014. Loss-of-function mutations in SLC30A8 protect against type 2 diabetes. Nat Genet 46, 357-363.

Gupta, S., Chai, J., Cheng, J., D'Mello, R., Chance, M.R., Fu, D., 2014. Visualizing the kinetic power stroke that drives proton-coupled zinc(II) transport. Nature 512, 101-104.

Ho, B.K., Gruswitz, F., 2008. HOLLOW: generating accurate representations of channel and interior surfaces in molecular structures. BMC Struct Biol 8, 49.

Hoch, E., Lin, W., Chai, J., Hershfinkel, M., Fu, D., Sekler, I., 2012. Histidine pairing at the metal transport site of mammalian ZnT transporters controls Zn2+ over Cd2+ selectivity. Proc Natl Acad Sci U S A 109, 7202-7207.

Hutton, J.C., 1982. The internal pH and membrane potential of the insulin-secretory granule. Biochem J 204, 171-178.

Jerabek-Willemsen, M., Wienken, C.J., Braun, D., Baaske, P., Duhr, S., 2011. Molecular interaction studies using microscale thermophoresis. Assay Drug Dev Technol 9, 342-353.

Kambe, T., Tsuji, T., Hashimoto, A., Itsumura, N., 2015. The Physiological, Biochemical, and Molecular Roles of Zinc Transporters in Zinc Homeostasis and Metabolism. Physiol Rev 95, 749-784.

Kawasaki, E., 2012. ZnT8 and type 1 diabetes. Endocr J 59, 531-537.

Llopis, J., McCaffery, J.M., Miyawaki, A., Farquhar, M.G., Tsien, R.Y., 1998. Measurement of cytosolic, mitochondrial, and Golgi pH in single living cells with green fluorescent proteins. Proc Natl Acad Sci U S A 95, 6803-6808.

Lopez-Redondo, M., Fan, S., Koide, A., Koide, S., Beckstein, O., Stokes, D.L., 2021. Zinc binding alters the conformational dynamics and drives the transport cycle of the cation diffusion facilitator YiiP. J Gen Physiol 153.

Lopez-Redondo, M.L., Coudray, N., Zhang, Z., Alexopoulos, J., Stokes, D.L., 2018. Structural basis for the alternating access mechanism of the cation diffusion facilitator YiiP. Proc Natl Acad Sci U S A 115, 3042-3047.

Lu, M., Fu, D., 2007. Structure of the zinc transporter YiiP. Science 317, 1746-1748.

Lu, M., Chai, J., Fu, D., 2009. Structural basis for autoregulation of the zinc transporter YiiP. Nat Struct Mol Biol 16, 1063-1067.

Maret, W., 2013. Zinc biochemistry: from a single zinc enzyme to a key element of life. Adv Nutr 4, 82-91.

Ohana, E., Hoch, E., Keasar, C., Kambe, T., Yifrach, O., Hershfinkel, M., Sekler, I., 2009. Identification of the Zn2+ binding site and mode of operation of a mammalian Zn2+ transporter. J Biol Chem 284, 17677-17686.

Pettersen, E.F., Goddard, T.D., Huang, C.C., Couch, G.S., Greenblatt, D.M., Meng, E.C., Ferrin, T.E., 2004. UCSF Chimera--a visualization system for exploratory research and analysis. J Comput Chem 25, 1605-1612.

Punjani, A., Zhang, H., Fleet, D.J., 2020. Non-uniform refinement: adaptive regularization improves single-particle cryo-EM reconstruction. Nat Methods 17, 1214-1221.

Punjani, A., Rubinstein, J.L., Fleet, D.J., Brubaker, M.A., 2017. cryoSPARC: algorithms for rapid unsupervised cryo-EM structure determination. Nat Methods 14, 290-296.

Saxena, R., Voight, B.F., Lyssenko, V., Burtt, N.P., de Bakker, P.I., Chen, H., Roix, J.J., Kathiresan, S., Hirschhorn, J.N., Daly, M.J., Hughes, T.E., Groop, L., Altshuler, D., Almgren, P., Florez, J.C., Meyer, J., Ardlie, K., Bengtsson Bostrom, K., Isomaa, B., Lettre, G., Lindblad, U., Lyon, H.N., Melander, O., Newton-Cheh, C., Nilsson, P., Orho-Melander, M., Rastam, L., Speliotes, E.K., Taskinen, M.R., Tuomi, T., Guiducci, C., Berglund, A., Carlson, J., Gianniny, L., Hackett, R., Hall, L., Holmkvist, J., Laurila, E., Sjogren, M., Sterner, M., Surti, A., Svensson, M., Svensson, M., Tewhey, R., Blumenstiel, B., Parkin, M., Defelice, M., Barry, R., Brodeur, W., Camarata, J., Chia, N., Fava, M., Gibbons, J., Handsaker, B., Healy, C., Nguyen, K., Gates, C., Sougnez, C., Gage, D., Nizzari, M., Gabriel, S.B., Chirn, G.W., Ma, Q., Parikh, H., Richardson, D., Ricke, D., Purcell, S., 2007. Genome-wide association analysis identifies loci for type 2 diabetes and triglyceride levels. Science 316, 1331-1336.

Scott, L.J., Mohlke, K.L., Bonnycastle, L.L., Willer, C.J., Li, Y., Duren, W.L., Erdos, M.R., Stringham, H.M., Chines, P.S., Jackson, A.U., Prokunina-Olsson, L., Ding, C.J., Swift, A.J., Narisu, N., Hu, T., Pruim, R., Xiao, R., Li, X.Y., Conneely, K.N., Riebow, N.L., Sprau, A.G., Tong, M., White, P.P., Hetrick, K.N., Barnhart, M.W., Bark, C.W., Goldstein, J.L., Watkins, L., Xiang, F., Saramies, J., Buchanan, T.A., Watanabe, R.M., Valle, T.T., Kinnunen, L., Abecasis, G.R., Pugh, E.W., Doheny, K.F., Bergman, R.N., Tuomilehto, J., Collins, F.S., Boehnke, M., 2007. A genome-wide association study of type 2 diabetes in Finns detects multiple susceptibility variants. Science 316, 1341-1345.

Shusterman, E., Beharier, O., Shiri, L., Zarivach, R., Etzion, Y., Campbell, C.R., Lee, I.H., Okabayashi, K., Dinudom, A., Cook, D.I., Katz, A., Moran, A., 2014. ZnT-1 extrudes zinc from mammalian cells functioning as a Zn(2+)/H(+) exchanger. Metallomics 6, 1656-1663.

Sladek, R., Rocheleau, G., Rung, J., Dina, C., Shen, L., Serre, D., Boutin, P., Vincent, D., Belisle, A., Hadjadj, S., Balkau, B., Heude, B., Charpentier, G., Hudson, T.J., Montpetit, A., Pshezhetsky, A.V., Prentki, M., Posner, B.I., Balding, D.J., Meyre, D., Polychronakos, C., Froguel, P., 2007. A genome-wide association study identifies novel risk loci for type 2 diabetes. Nature 445, 881-885.

Stiernet, P., Nenquin, M., Moulin, P., Jonas, J.C., Henquin, J.C., 2007. Glucose-induced cytosolic pH changes in beta-cells and insulin secretion are not causally related: studies in islets lacking the Na+/H+ exchangeR NHE1. J Biol Chem 282, 24538-24546.

Thompson, J.D., Higgins, D.G., Gibson, T.J., 1994. CLUSTAL W: improving the sensitivity of progressive multiple sequence alignment through sequence weighting, position-specific gap penalties and weight matrix choice. Nucleic Acids Res 22, 4673-4680.

Vallee, B.L., Falchuk, K.H., 1993. The biochemical basis of zinc physiology. Physiol Rev 73, 79-118.

Wenzlau, J.M., Juhl, K., Yu, L., Moua, O., Sarkar, S.A., Gottlieb, P., Rewers, M., Eisenbarth, G.S., Jensen, J., Davidson, H.W., Hutton, J.C., 2007. The cation efflux transporter ZnT8 (Slc30A8) is a major autoantigen in human type 1 diabetes. Proc Natl Acad Sci U S A 104, 17040-17045.

Xue, J., Xie, T., Zeng, W., Jiang, Y., Bai, X.C., 2020. Cryo-EM structures of human ZnT8 in both outward- and inward-facing conformations. Elife 9.

Zeggini, E., Weedon, M.N., Lindgren, C.M., Frayling, T.M., Elliott, K.S., Lango, H., Timpson, N.J., Perry, J.R., Rayner, N.W., Freathy, R.M., Barrett, J.C., Shields, B., Morris, A.P., Ellard, S.,

Groves, C.J., Harries, L.W., Marchini, J.L., Owen, K.R., Knight, B., Cardon, L.R., Walker, M., Hitman, G.A., Morris, A.D., Doney, A.S., Wellcome Trust Case Control, C., McCarthy, M.I., Hattersley, A.T., 2007. Replication of genome-wide association signals in UK samples reveals risk loci for type 2 diabetes. Science 316, 1336-1341.

Zhang, K., 2016. Gctf: Real-time CTF determination and correction. J Struct Biol 193, 1-12.

Zheng, S.Q., Palovcak, E., Armache, J.P., Verba, K.A., Cheng, Y., Agard, D.A., 2017. MotionCor2: anisotropic correction of beam-induced motion for improved cryo-electron microscopy. Nat Methods 14, 331-332.

Zivanov, J., Nakane, T., Forsberg, B.O., Kimanius, D., Hagen, W.J., Lindahl, E., Scheres, S.H., 2018. New tools for automated high-resolution cryo-EM structure determination in RELION-3. Elife 7.

Table 1. Cryo-EM data collection and model statistics.

	xtZnT8-Zn^{2+} (EMD-33619) (PDB: 7Y5G)	xtZnT8-H^{+} (EMD-33620) (PDB: 7Y5H)
Data collection and processing		
Magnification	130,000	165,000
Voltage (kV)	300	300
Electron exposure (e^{-}/Å^2)	50.1	63.9
Defocus range (μm)	-1.0~-1.7	-1.1~-1.7
Pixel size (Å)	1.1	0.85
Symmetry imposed	C2	C2
Initial particle images (no.)	928,822	684,578
Final particle images (no.)	233,408	101,706
Map resolution (Å)	3.85	3.72
FSC threshold	0.143	0.143
Refinement		
Model composition		
Non-hydrogen atoms	4736	4704
Protein residues	604	600
Ligands	6	4
R.m.s. deviations		
Bond lengths (Å)	0.002	0.002
Bond angles (°)	0.433	0.391
Validation		
MolProbity score	1.01	1.16
Clashscore	2.29	3.76
Rotamer outliers (%)	0.00	0.00
Ramachandran plot		
Favored (%)	99.32	99.49
Allowed (%)	0.68	0.51
Disallowed (%)	0.00	0.00
B-factors (Å^2)		
Protein	28.11	41.22
Ligand	48.60	65.00

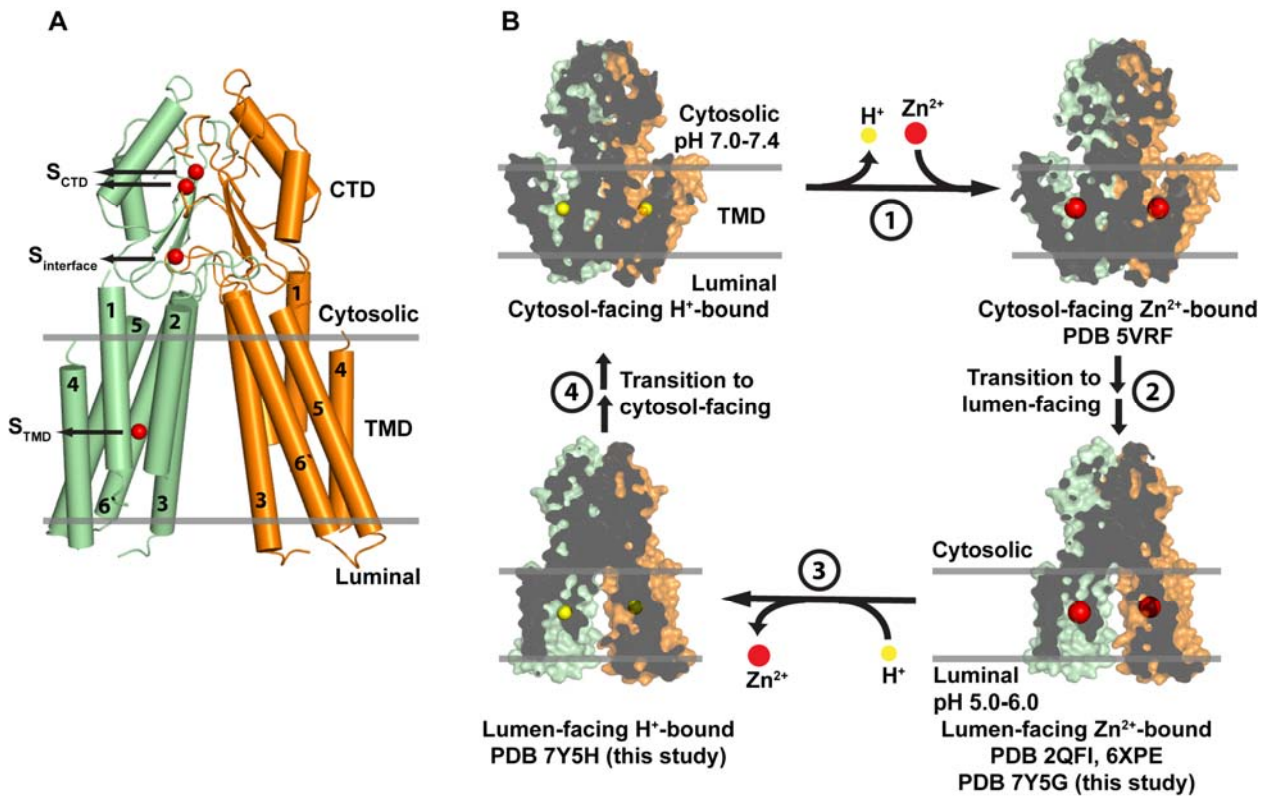

Figure 1. Structure and a working model for Zn^{2+} transport in ZnT8. (A) Cryo-EM structure of hZnT8 in the presence of Zn^{2+} in a lumen-facing conformation (PDB: 6XPE). The hZnT8 dimer is displayed in cartoon mode with two protomers colored in green and orange, respectively. Bound Zn^{2+} are rendered as red spheres in one protomer only for better viewing. Transmembrane segments of each protomer are numbered from one to six. The relative position of the granule membrane is indicated by two grey lines. (B) A simplified alternating-access model for ZnT8. The dimeric ZnT8 models are displayed in surface mode with two protomers colored in green and orange, respectively. S_{TMD}-bound H^+/Zn^{2+} are rendered as spheres as indicated.

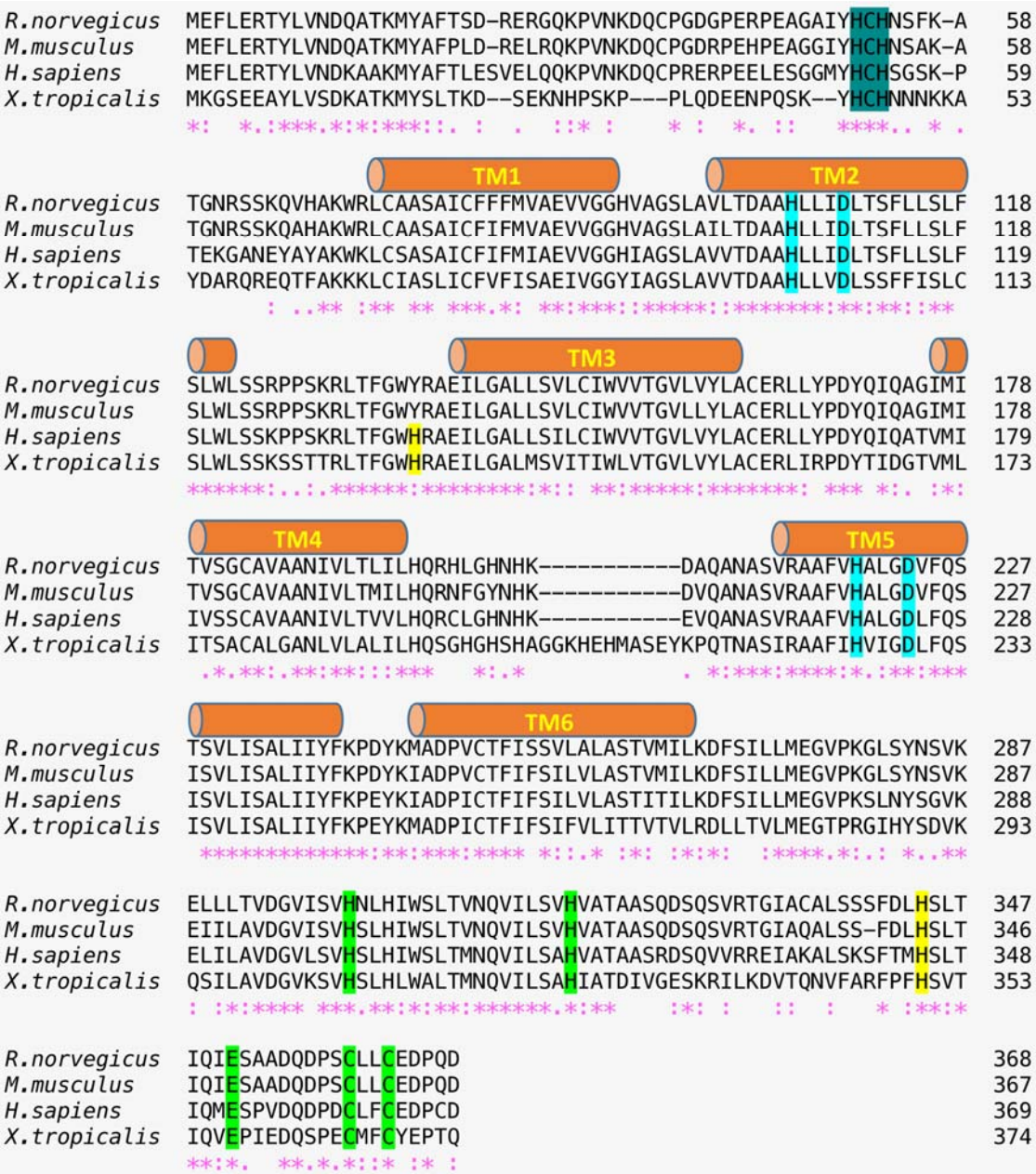

Figure 2. Sequence alignment of ZnT8 homologs by ClustalW (Combet et al., 2000; Thompson et al., 1994). Transmembrane segments are indicated by cylinders and labeled from TM1 to TM6. The S_{TMD} site residues are highlighted in cyan, the S_{CTD} sites in green (including the HCH motif in dark green), and the $S_{interface}$ site in yellow. Asterisks (*) indicate identical residues. Colons (:) indicate strong similarities. Periods (.) indicate weak similarities. *R. norvegicus*, *Rattus norvegicus*; *M. musculus*, *Mus musculus*; *H. sapiens*, *Homo sapiens*; *X. tropicalis*, *Xenopus tropicalis*.

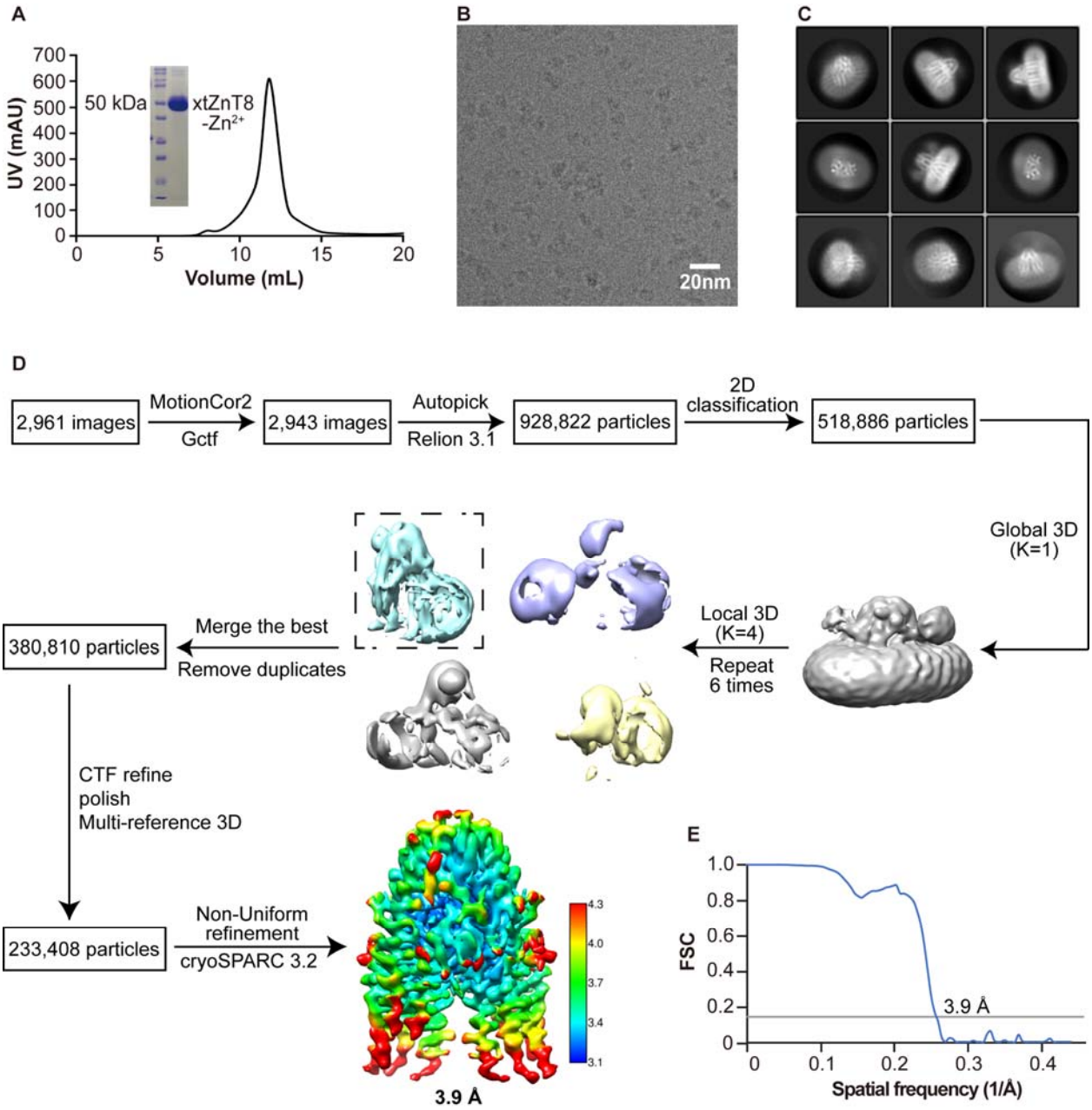

Figure 3. Cryo-EM sample preparation and data processing of xtZnT8-Zn^{2+}. (A) The elution profile of xtZnT8-Zn^{2+} in the presence of 1 mM Zn^{2+} at pH 7.5 on a size-exclusion column. The insert shows SDS-PAGE analysis of the purified sample. (B) A representative area of cryo-EM micrographs of xtZnT8-Zn^{2+} particles. (C) Selected 2D class averages of xtZnT8-Zn^{2+} particles. (D) The workflow of cryo-EM data processing of the xtZnT8-Zn^{2+} dataset. (E) The overall resolution of xtZnT8-Zn^{2+} was determined by the "gold standard" FSC curve using the FSC=0.143 criterion.

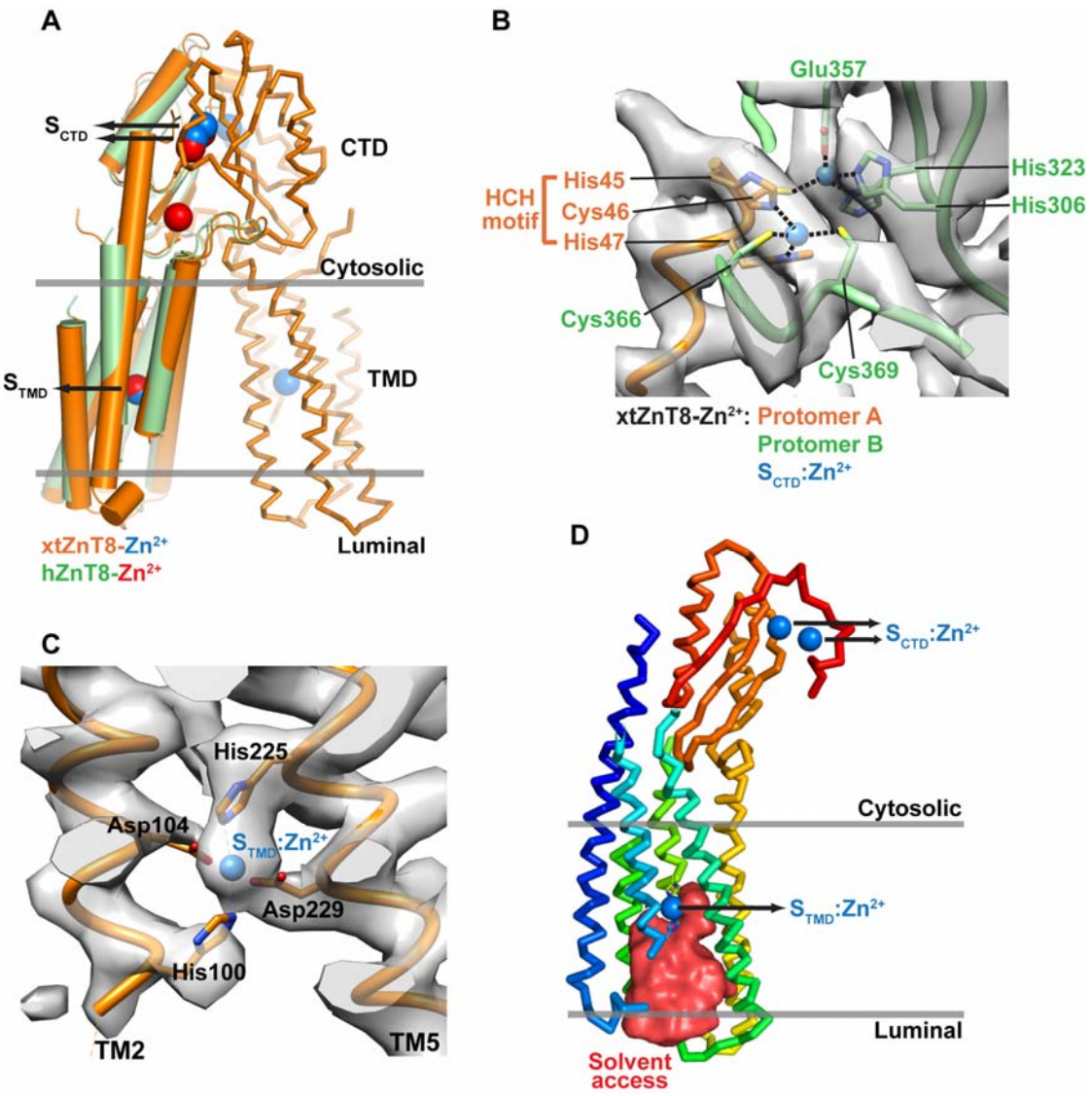

Figure 4. Cryo-EM structure of xtZnT8-Zn^{2+} in a lumen-facing state. (A) The xtZnT8-Zn^{2+} dimer is displayed in orange, with one protomer in cartoon mode and the other as ribbons. Bound Zn^{2+} are shown as blue spheres. One protomer of the hZnT8-Zn^{2+} structure (PDB: 6XPE) is displayed in green with bound Zn^{2+} rendered as red spheres, and is superimposed onto xtZnT8-Zn^{2+}. The relative position of the granule membrane is indicated by two grey lines. (B) The S_{CTD} sites of xtZnT8-Zn^{2+}. Two protomers are displayed as ribbons with one in orange and the other in green. The S_{CTD}-bound Zn^{2+} are shown as blue spheres. The Zn^{2+}-coordinating residues are displayed as sticks, and the HCH motif is indicated. The cryo-EM map of xtZnT8-Zn^{2+} is shown as grey densities. (C) One Zn^{2+} (blue sphere) binds to the S_{TMD} site in xtZnT8-Zn^{2+}. The Zn^{2+}-coordinating residues are displayed as sticks. The cryo-EM map of xtZnT8-Zn^{2+} is shown as grey

densities. (D) One protomer of xtZnT8-Zn^{2+} is displayed as ribbons, which is colored in rainbow spectrum with blue for the amino-terminus. Bound Zn^{2+} are shown as blue spheres. The solvent-accessible space is shown as a red surface. The relative position of the granule membrane is indicated by two grey lines.

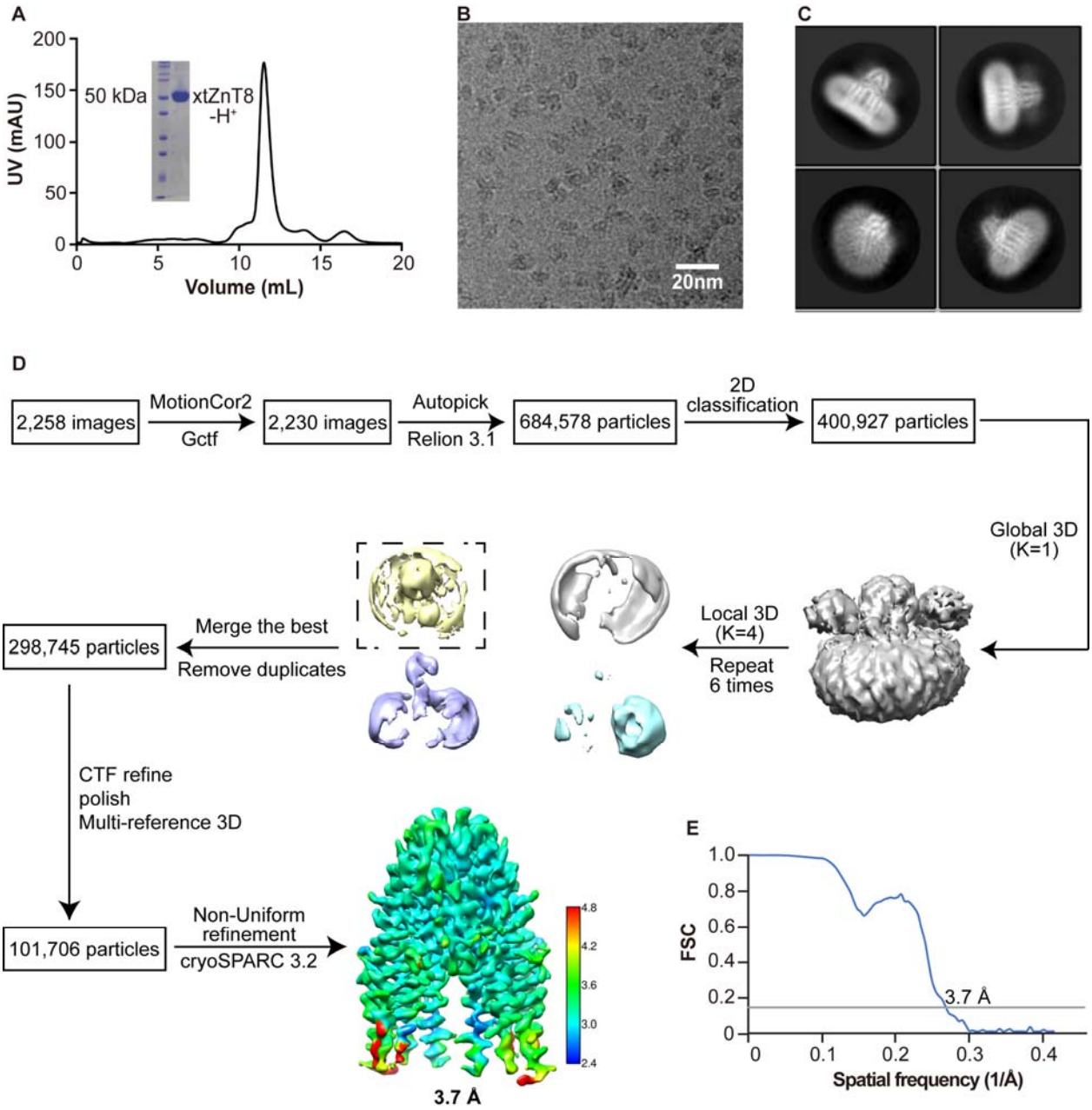

Figure 5. Cryo-EM sample preparation and data processing of xtZnT8-H$^+$. (A) The elution profile of xtZnT8-H$^+$ in the presence of 1 mM Zn^{2+} at pH 5.5 on a size-exclusion column. The insert shows SDS-PAGE analysis of the purified sample. (B) A representative area of cryo-EM micrographs of xtZnT8-H$^+$ particles. (C) Selected 2D class averages of xtZnT8-H$^+$ particles. (D) The workflow of cryo-EM data processing of the xtZnT8-H$^+$ dataset. (E) The overall resolution of xtZnT8-H$^+$ was determined by the "gold standard" FSC curve using the FSC=0.143 criterion.

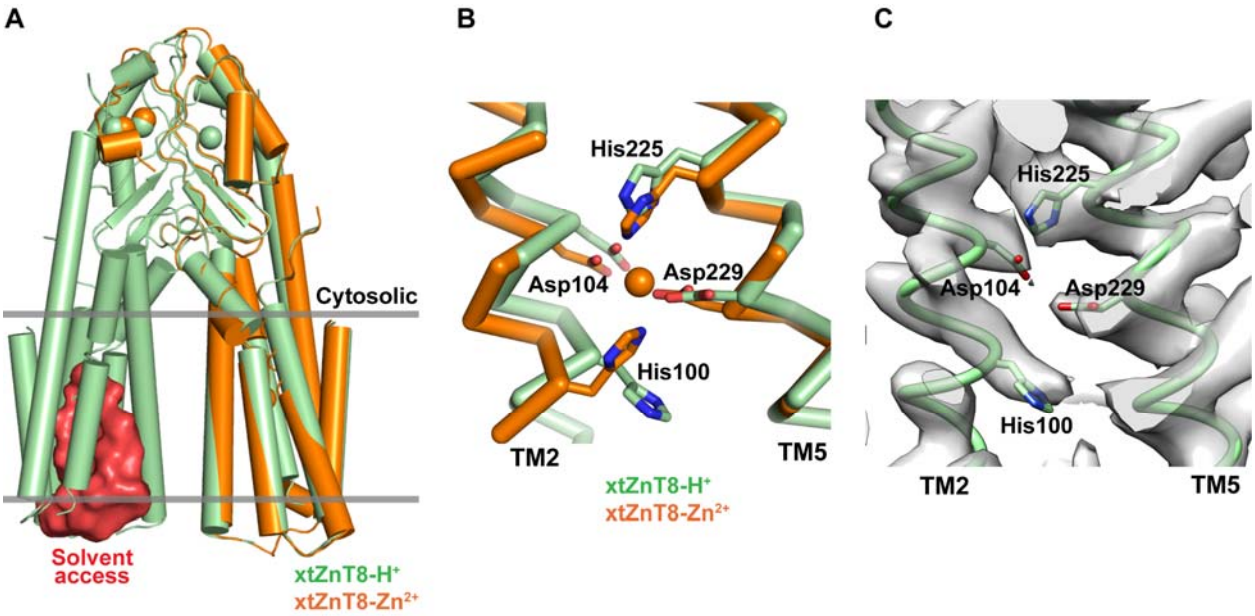

Figure 6. Cryo-EM structure of xtZnT8-H$^+$ in a lumen-facing state. (A) The xtZnT8-H$^+$ dimer is displayed in green, with a red surface indicating the solvent-accessible space for one protomer. One protomer of the xtZnT8-Zn^{2+} structure is displayed in orange and is superimposed onto xtZnT8-H$^+$. Bound Zn^{2+} are shown as spheres. The relative position of the granule membrane is indicated by two grey lines. (B) Comparison of the S_{TMD} site between xtZnT8-H$^+$ (in green) and xtZnT8-Zn^{2+} (in orange). One Zn^{2+} (orange sphere) binds to S_{TMD} in xtZnT8-Zn^{2+}. The Zn^{2+}-coordinating residues are rendered as sticks. (C) The cryo-EM density map of the S_{TMD} site in xtZnT8-H$^+$. The Zn^{2+}-coordinating residues are rendered as sticks.

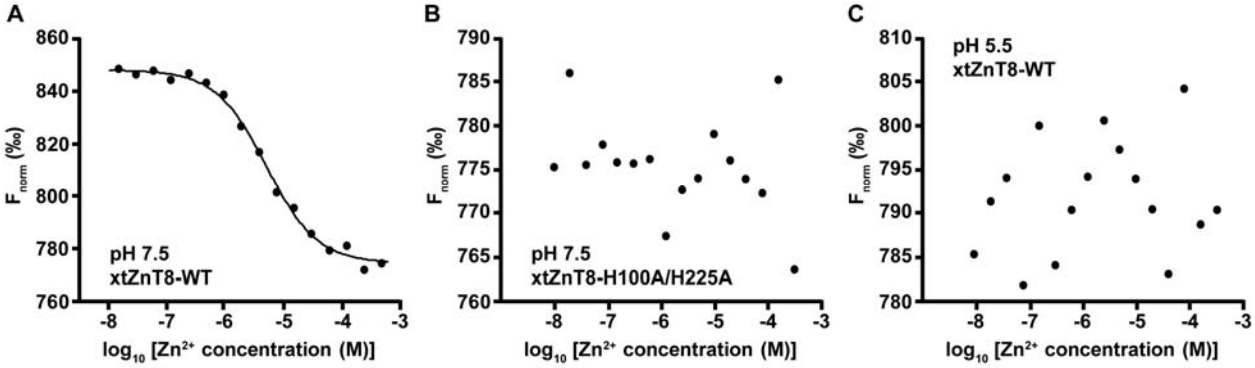

Figure 7. Binding of Zn^{2+} to xtZnT8 measured by microscale thermophoresis. (A) A representative MST curve for wild-type xtZnT8 (xtZnT8-WT) titrated with Zn^{2+} at pH 7.5. (B) A representative MST measurement for an S_{TMD}-double-mutant of xtZnT8 (xtZnT8-H100A/H225A) titrated with Zn^{2+} at pH 7.5. (C) A representative MST measurement for wild-type xtZnT8 titrated with Zn^{2+} at pH 5.5. The detailed procedure of MST measurements were described in the "Materials and methods" section.

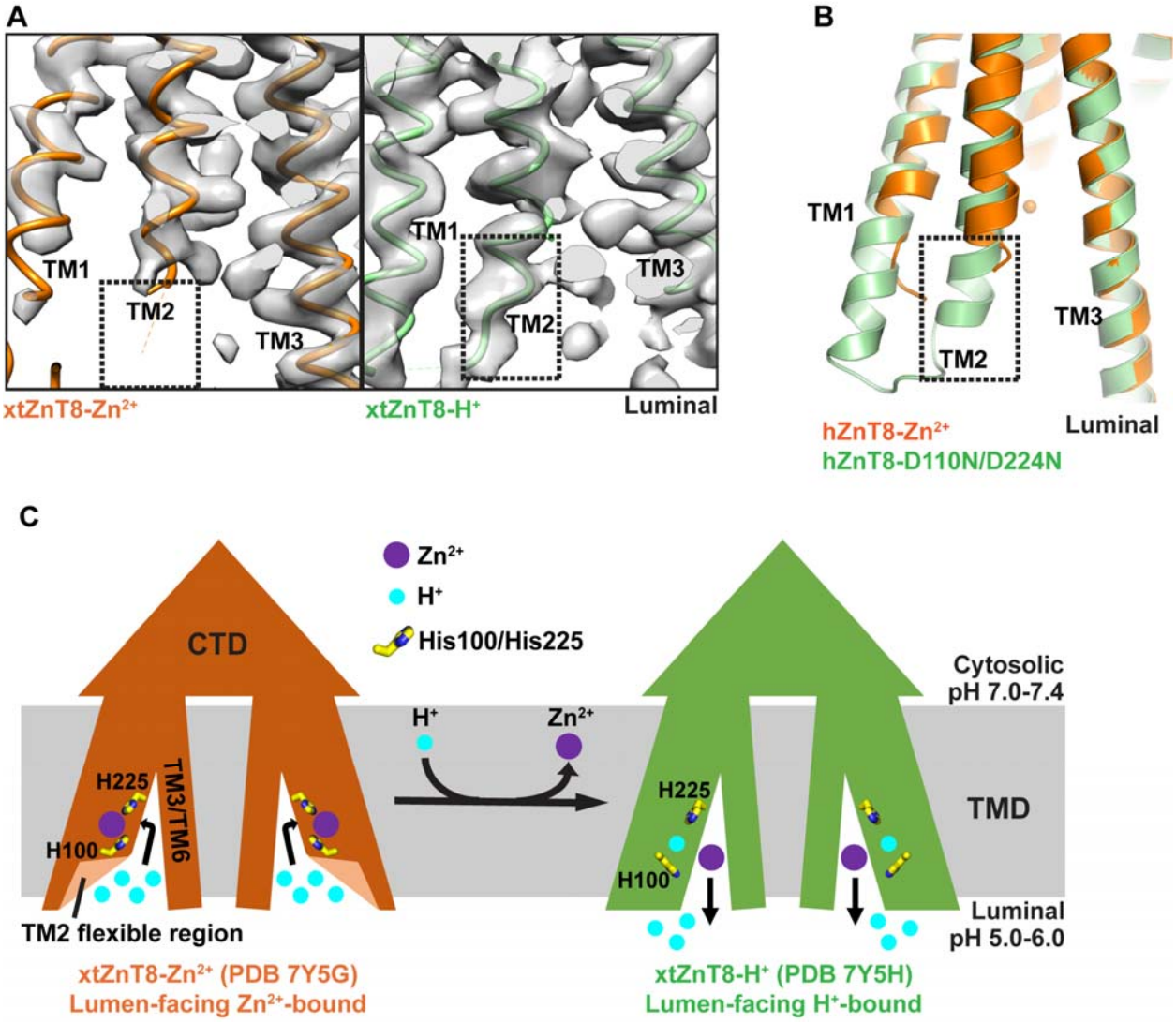

Figure 8. A potential Zn^{2+}-releasing mechanism in ZnT8. (A) Comparison of the cryo-EM density maps between xtZnT8-Zn^{2+} (orange ribbons, left) and xtZnT8-H^+ (green ribbons, right) for a TM2 region near the luminal side (boxed). (B) Structural comparison between hZnT8-Zn^{2+} (orange ribbons) and hZnT8-D110N/D224N (green ribbons) for a TM2 region near the luminal side (boxed). (C) A H^+-facilitated Zn^{2+}-releasing mechanism is proposed for ZnT8 based on xtZnT8-Zn^{2+} and xtZnT8-H^+ structures. Briefly, in the Zn^{2+}-bound lumen-facing state of ZnT8, a flexible TM2 region near the luminal side increases access of luminal protons to the S_{TMD} site. Protonation of S_{TMD}, likely through the two histidine residues, disrupts Zn^{2+} coordination and facilitates Zn^{2+} release from S_{TMD} to the lumen. For better viewing, the other two aspartate residues of the S_{TMD} site (D104/D229) were not displayed.

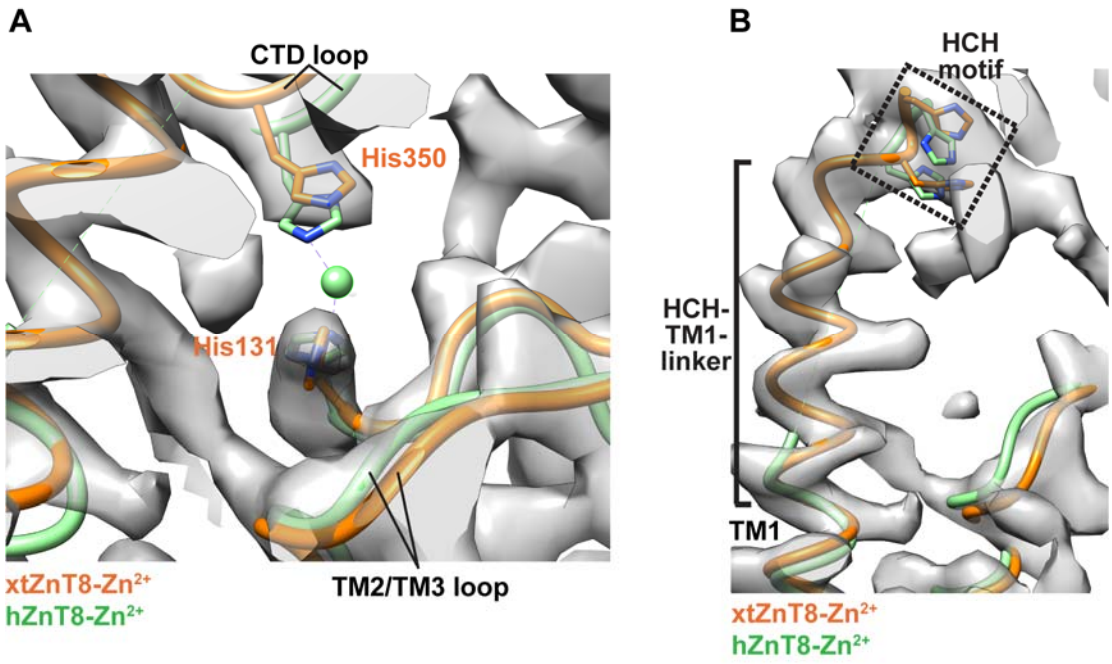

Figure 9. Differences between xtZnT8-Zn^{2+} and hZnT8-Zn^{2+} structures. (A) Comparison of the $S_{interface}$ site. The cryo-EM density map for the $S_{interface}$ site of xtZnT8-Zn^{2+} (orange ribbons) formed by His131 and His350 (orange sticks), corresponding to His137 and His345 (green sticks) in hZnT8-Zn^{2+} (green ribbons). The $S_{interface}$-bound Zn^{2+} in hZnT8-Zn^{2+} is rendered as a green sphere. No Zn^{2+} density was present at the $S_{interface}$ site of xtZnT8-Zn^{2+}. (B) The cryo-EM density map of HCH-TM1-linker in xtZnT8-Zn^{2+}. The xtZnT8-Zn^{2+} structure is displayed as orange ribbons, and the hZnT8-Zn^{2+} structure (green ribbons) is superimposed onto xtZnT8-Zn^{2+}. The HCH motif is boxed and indicated.

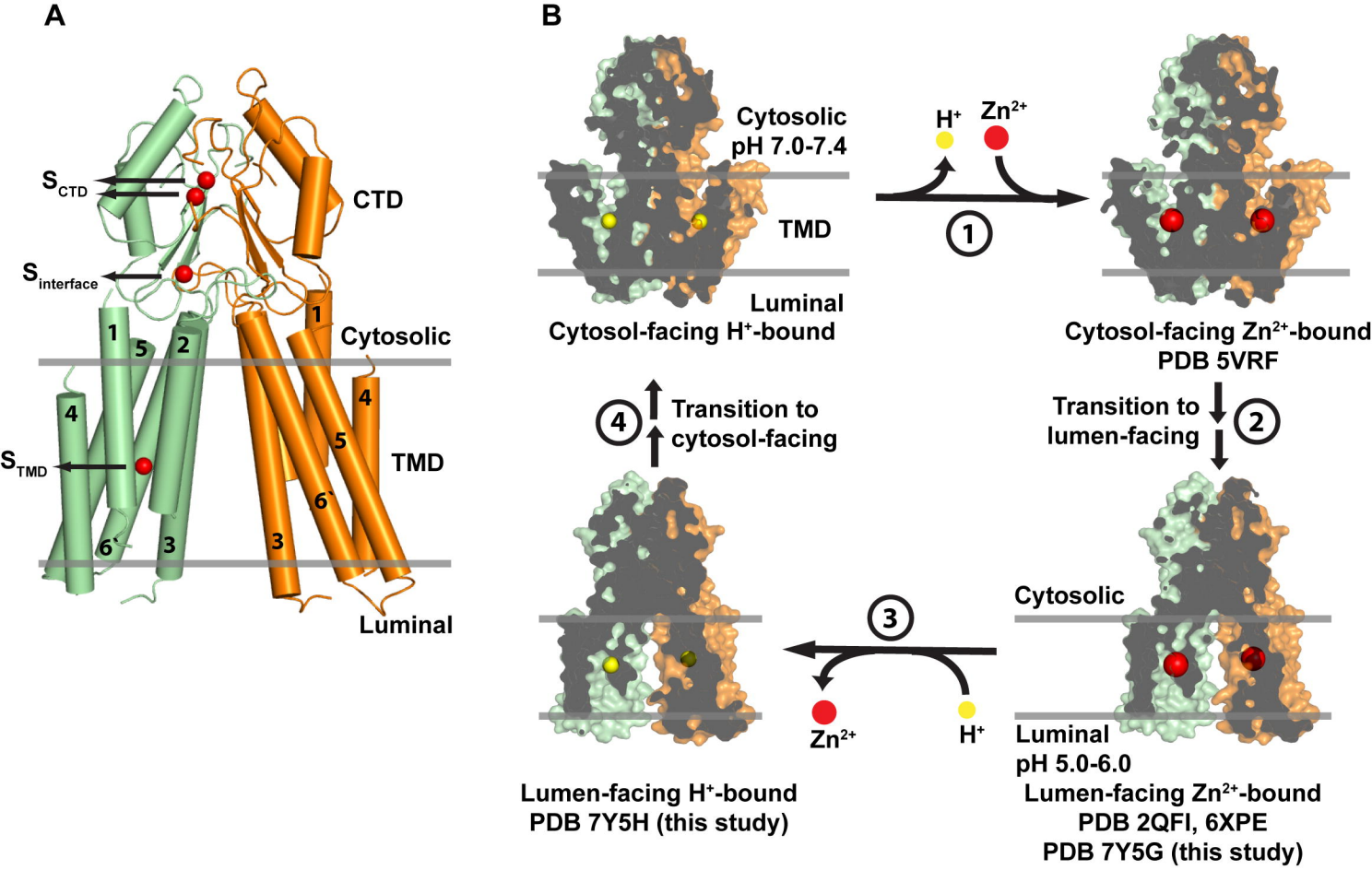
A
S CTD
S interface
S TMD
CTD
Cytosolic
TMD
Luminal
1
2
3
4
5
6
B
Cytosolic
pH 7.0-7.4
TMD
Luminal
Cytosol-facing H+-bound
H+
Zn2+
1
Cytosol-facing Zn2+-bound
PDB 5VRF
Transition to
lumen-facing
2
Cytosolic
Luminal
pH 5.0-6.0
Lumen-facing Zn2+-bound
PDB 2QFI, 6XPE
PDB 7Y5G (this study)
3
Zn2+
H+
Lumen-facing H+-bound
PDB 7Y5H (this study)
4
Transition to
cytosol-facing

```
R.norvegicus   MEFLERTYLVNDQATKMYAFTSD-RERGQKPVNKDQCPGDGPERPEAGAIYHCHNSFK-A   58
M.musculus     MEFLERTYLVNDQATKMYAFPLD-RELRQKPVNKDQCPGDRPEHPEAGGIYHCHNSAK-A   58
H.sapiens      MEFLERTYLVNDKAAKMYAFTLESVELQQKPVNKDQCPRERPEELESGGMYHCHSGSK-P   59
X.tropicalis   MKGSEEAYLVSDKATKMYSLTKD--SEKNHPSKP---PLQDEENPQSK--YHCHNNNKKA   53
               *:  *.:***.*:*:***::. :  .  ::* :    * :  *. ::   ****.. * .

                                TM1                    TM2
R.norvegicus   TGNRSSKQVHAKWRLCAASAICFFFMVAEVVGGHVAGSLAVLTDAAHLLIDLTSFLLSLF  118
M.musculus     TGNRSSKQAHAKWRLCAASAICFIFMVAEVVGGHVAGSLAILTDAAHLLIDLTSFLLSLF  118
H.sapiens      TEKGANEYAYAKWKLCSASAICFIFMIAEVVGGHIAGSLAVVTDAAHLLIDLTSFLLSLF  119
X.tropicalis   YDARQREQTFAKKKLCIASLICFVFISAEIVGGYIAGSLAVVTDAAHLLVDLSSFFISLC  113
                     : ..** :** ** ***.*: **:***::*****::*******:**:**::**

                                TM3
R.norvegicus   SLWLSSRPPSKRLTFGWYRAEILGALLSVLCIWVVTGVLVYLACERLLYPDYQIQAGIMI  178
M.musculus     SLWLSSRPPSKRLTFGWYRAEILGALLSVLCIWVVTGVLLYLACERLLYPDYQIQAGIMI  178
H.sapiens      SLWLSSKPPSKRLTFGWHRAEILGALLSILCIWVVTGVLVYLACERLLYPDYQIQATVMI  179
X.tropicalis   SLWLSSKSSTTRLTFGWHRAEILGALMSVITIWLVTGVLVYLACERLIRPDYTIDGTVML  173
               ******:..:.******:********:*:: **:*****:*******: *** *:. :*:

                TM4                                          TM5
R.norvegicus   TVSGCAVAANIVLTLILHQRHLGHNHK-----------DAQANASVRAAFVHALGDVFQS  227
M.musculus     TVSGCAVAANIVLTMILHQRNFGYNHK-----------DVQANASVRAAFVHALGDVFQS  227
H.sapiens      IVSSCAVAANIVLTVVLHQRCLGHNHK-----------EVQANASVRAAFVHALGDLFQS  228
X.tropicalis   ITSACALGANLVLALILHQSGHGHSHAGGKHEHMASEYKPQTNASIRAAFIHVIGDLFQS  233
                .*.**:.**:**:::***   *:.*            . *:***:****:*.:**:***

                                TM6
R.norvegicus   TSVLISALIIYFKPDYKMADPVCTFISSVLALASTVMILKDFSILLMEGVPKGLSYNSVK  287
M.musculus     ISVLISALIIYFKPDYKIADPVCTFIFSILVLASTVMILKDFSILLMEGVPKGLSYNSVK  287
H.sapiens      ISVLISALIIYFKPEYKIADPICTFIFSILVLASTITILKDFSILLMEGVPKSLNYSGVK  288
X.tropicalis   ISVLISALIIYFKPEYKMADPICTFIFSIFVLITTVTVLRDLLTVLMEGTPRGIHYSDVK  293
                **************:**:***:**** *::.* :*: :*:*:  :****.*:.: *..**

R.norvegicus   ELLLTVDGVISVHNLHIWSLTVNQVILSVHVATAASQDSQSVRTGIACALSSSFDLHSLT  347
M.musculus     EIILAVDGVISVHSLHIWSLTVNQVILSVHVATAASQDSQSVRTGIAQALSS-FDLHSLT  346
H.sapiens      ELILAVDGVLSVHSLHIWSLTMNQVILSAHVATAASRDSQVVRREIAKALSKSFTMHSLT  348
X.tropicalis   QSILAVDGVKSVHSLHLWALTMNQVILSAHIATDIVGESKRILKDVTQNVFARFPFHSVT  353
               : :*:**** ***.**:*:**:******.*:**    :*: :   ::  :   * :**:*

R.norvegicus   IQIESAADQDPSCLLCEDPQD                                        368
M.musculus     IQIESAADQDPSCLLCEDPQD                                        367
H.sapiens      IQMESPVDQDPDCLFCEDPCD                                        369
X.tropicalis   IQVEPIEDQSPECMFCYEPTQ                                        374
               **:*.  **.*.*::* :* :
```

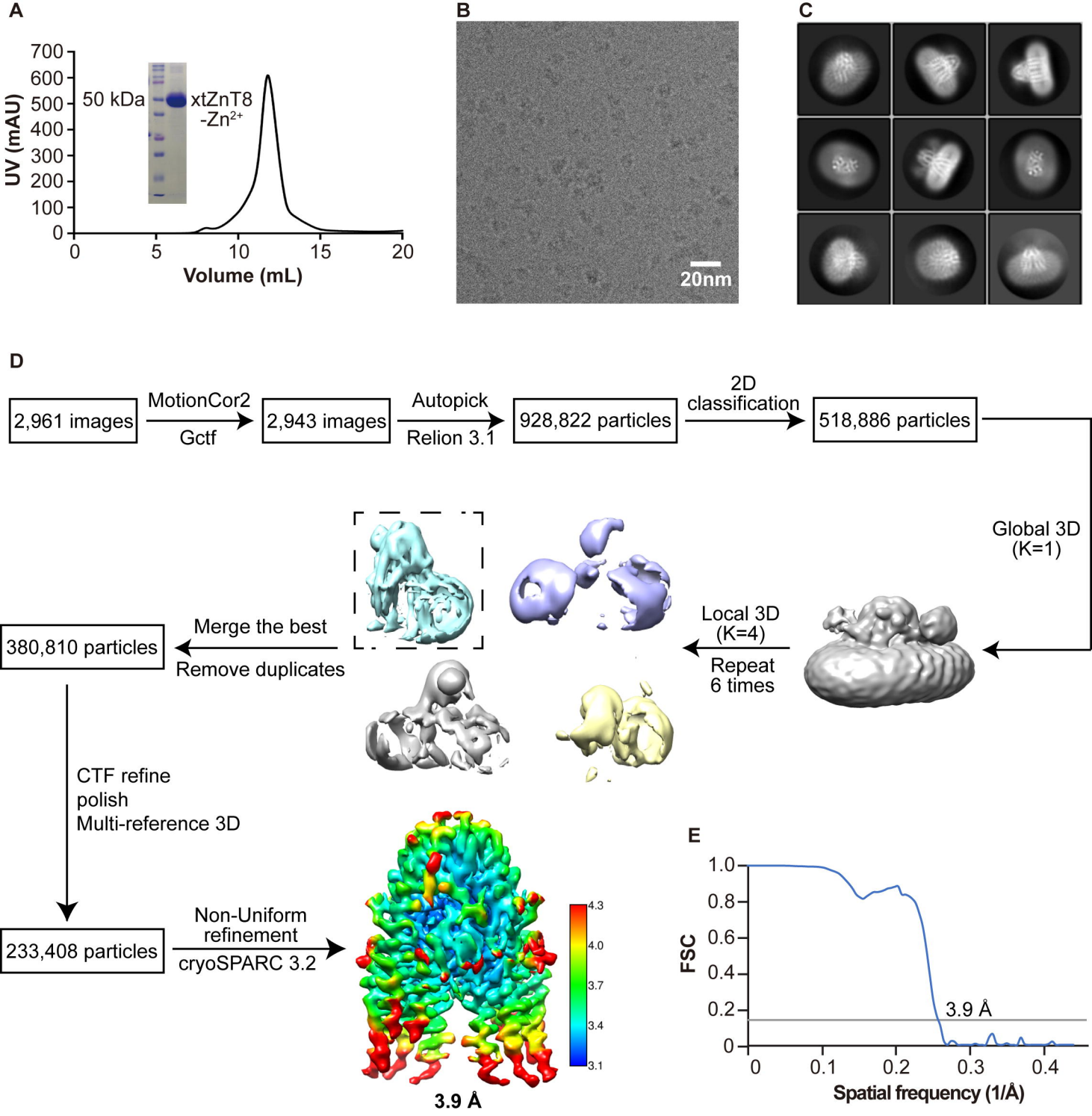
A
UV (mAU)
700
600
500
400
300
200
100
0
50 kDa
xtZnT8
-Zn2+
0
5
10
15
20
Volume (mL)
B
20nm
C
D
2,961 images
MotionCor2
Gctf
2,943 images
Autopick
Relion 3.1
928,822 particles
2D
classification
518,886 particles
Global 3D
(K=1)
Local 3D
(K=4)
Repeat
6 times
Merge the best
Remove duplicates
380,810 particles
CTF refine
polish
Multi-reference 3D
233,408 particles
Non-Uniform
refinement
cryoSPARC 3.2
4.3
4.0
3.7
3.4
3.1
3.9 Å
E
FSC
1.0
0.8
0.6
0.4
0.2
0
3.9 Å
0
0.1
0.2
0.3
0.4
Spatial frequency (1/Å)

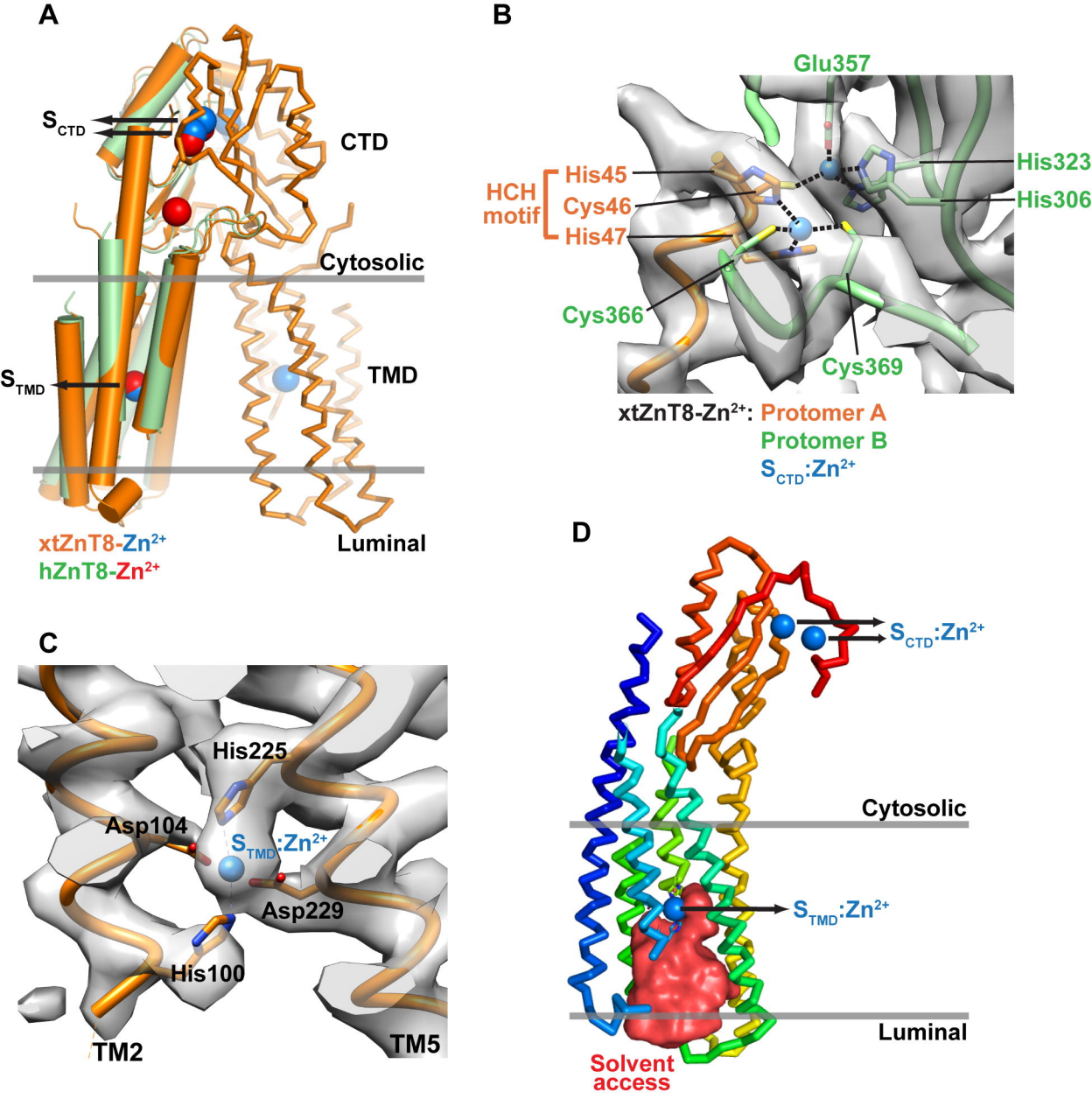
A
S_{CTD}
CTD
Cytosolic
S_{TMD}
TMD
Luminal
xtZnT8-Zn^{2+}
hZnT8-Zn^{2+}
B
Glu357
His45
HCH motif
Cys46
His47
His323
His306
Cys366
Cys369
xtZnT8-Zn^{2+}: Protomer A
Protomer B
S_{CTD}:Zn^{2+}
C
His225
Asp104
S_{TMD}:Zn^{2+}
Asp229
His100
TM2
TM5
D
S_{CTD}:Zn^{2+}
Cytosolic
S_{TMD}:Zn^{2+}
Luminal
Solvent access

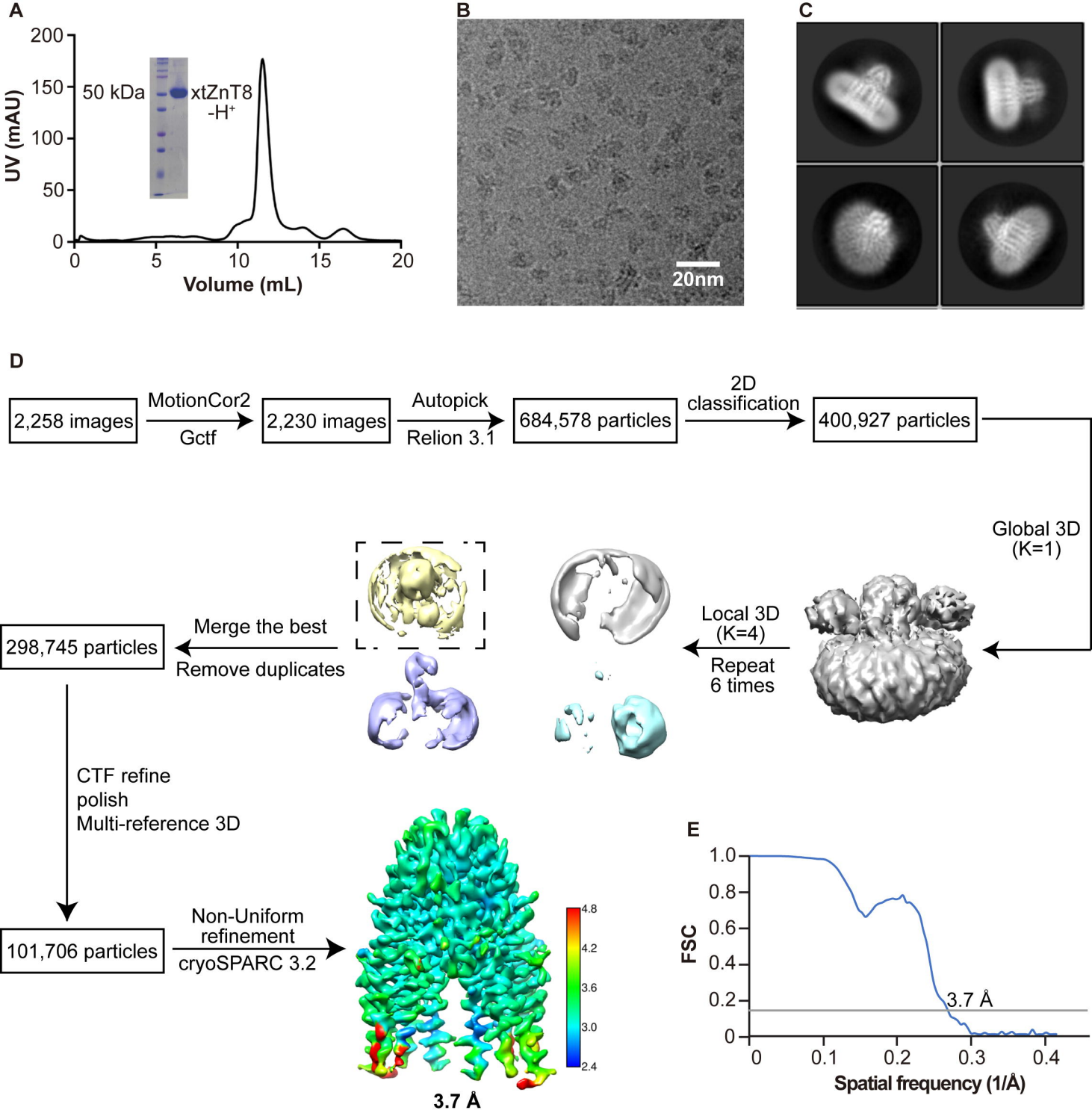
A
200
150
100
50
0
UV (mAU)
50 kDa
xtZnT8
-H+
0
5
10
15
20
Volume (mL)
B
20nm
C
D
2,258 images
MotionCor2
Gctf
2,230 images
Autopick
Relion 3.1
684,578 particles
2D
classification
400,927 particles
Global 3D
(K=1)
Local 3D
(K=4)
Repeat
6 times
Merge the best
Remove duplicates
298,745 particles
CTF refine
polish
Multi-reference 3D
101,706 particles
Non-Uniform
refinement
cryoSPARC 3.2
4.8
4.2
3.6
3.0
2.4
3.7 Å
E
1.0
0.8
0.6
0.4
0.2
0
FSC
3.7 Å
0
0.1
0.2
0.3
0.4
Spatial frequency (1/Å)

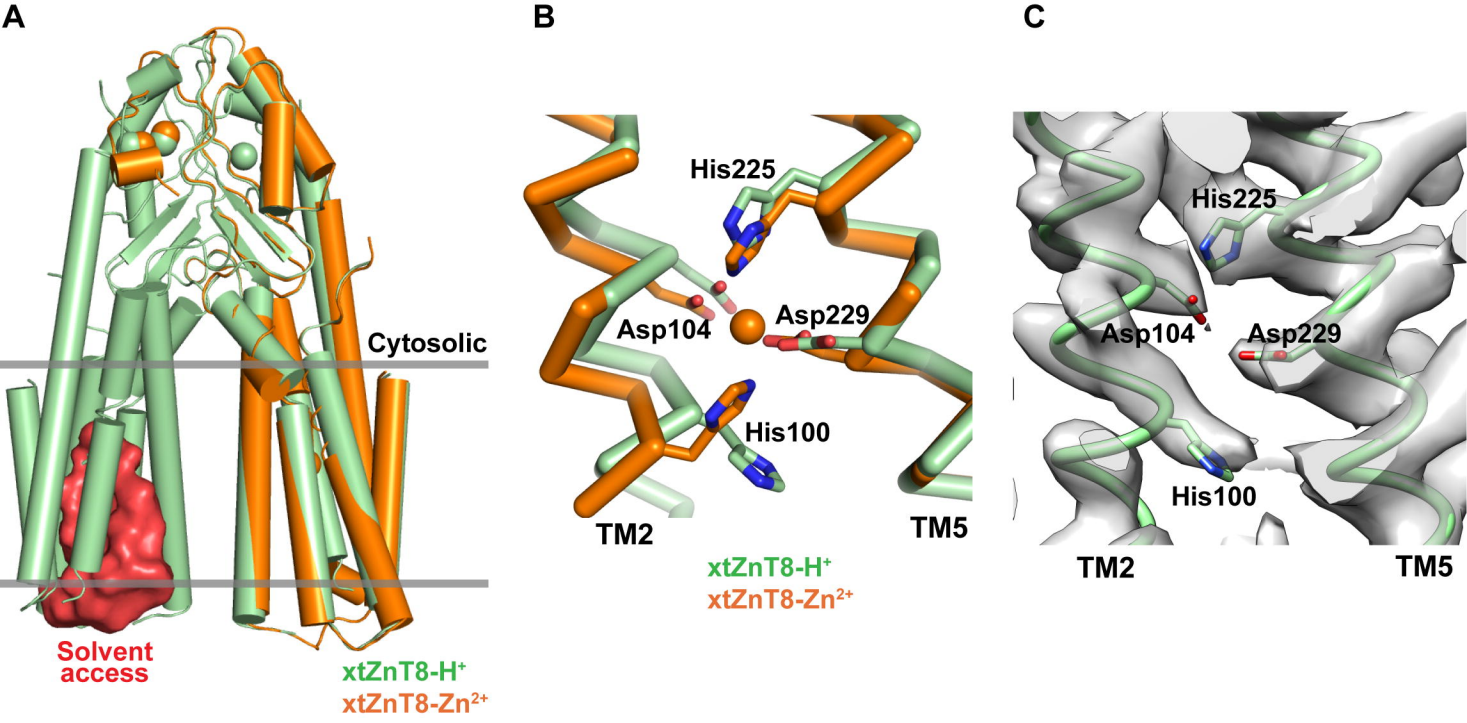
A
Cytosolic
Solvent access
xtZnT8-H+
xtZnT8-Zn2+
B
His225
Asp104
Asp229
His100
TM2
TM5
xtZnT8-H+
xtZnT8-Zn2+
C
His225
Asp104
Asp229
His100
TM2
TM5

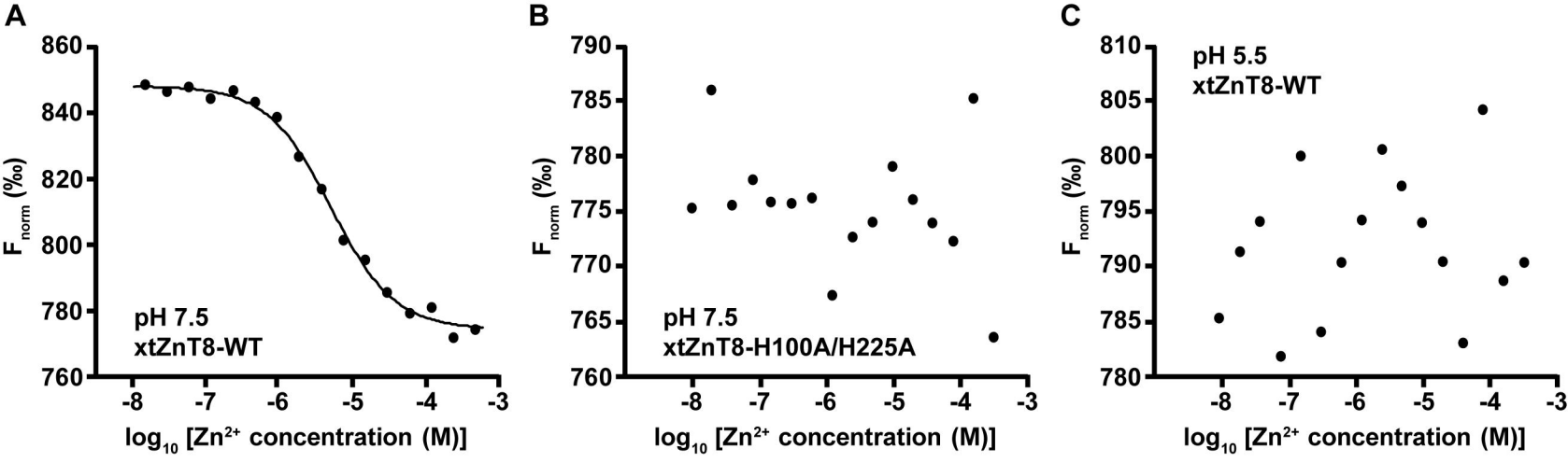
A
860
840
820
800
780
760
F_{norm} (‰)
pH 7.5
xtZnT8-WT
-8
-7
-6
-5
-4
-3
$\log_{10}$ [Zn^{2+} concentration (M)]
B
790
785
780
775
770
765
760
F_{norm} (‰)
pH 7.5
xtZnT8-H100A/H225A
-8
-7
-6
-5
-4
-3
$\log_{10}$ [Zn^{2+} concentration (M)]
C
810
805
800
795
790
785
780
F_{norm} (‰)
pH 5.5
xtZnT8-WT
-8
-7
-6
-5
-4
-3
$\log_{10}$ [Zn^{2+} concentration (M)]

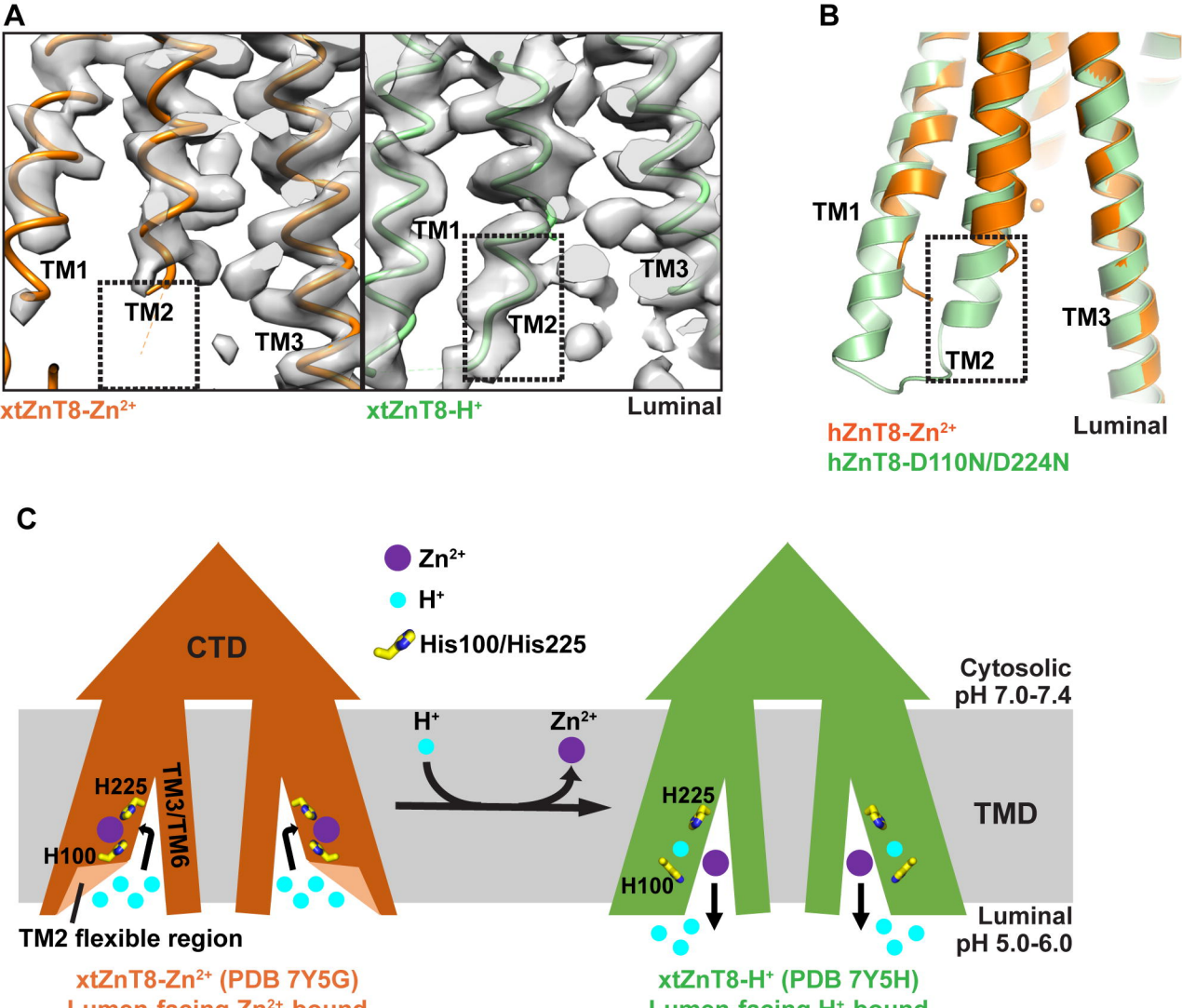
A
TM1
TM2
TM3
xtZnT8-Zn2+
TM1
TM2
TM3
xtZnT8-H+
Luminal
B
TM1
TM2
TM3
hZnT8-Zn2+
hZnT8-D110N/D224N
Luminal
C
Zn2+
H+
His100/His225
CTD
Cytosolic
pH 7.0-7.4
H+
Zn2+
H225
TM3/TM6
H100
TM2 flexible region
H225
H100
TMD
Luminal
pH 5.0-6.0
xtZnT8-Zn2+ (PDB 7Y5G)
Lumen-facing Zn2+-bound
xtZnT8-H+ (PDB 7Y5H)
Lumen-facing H+-bound

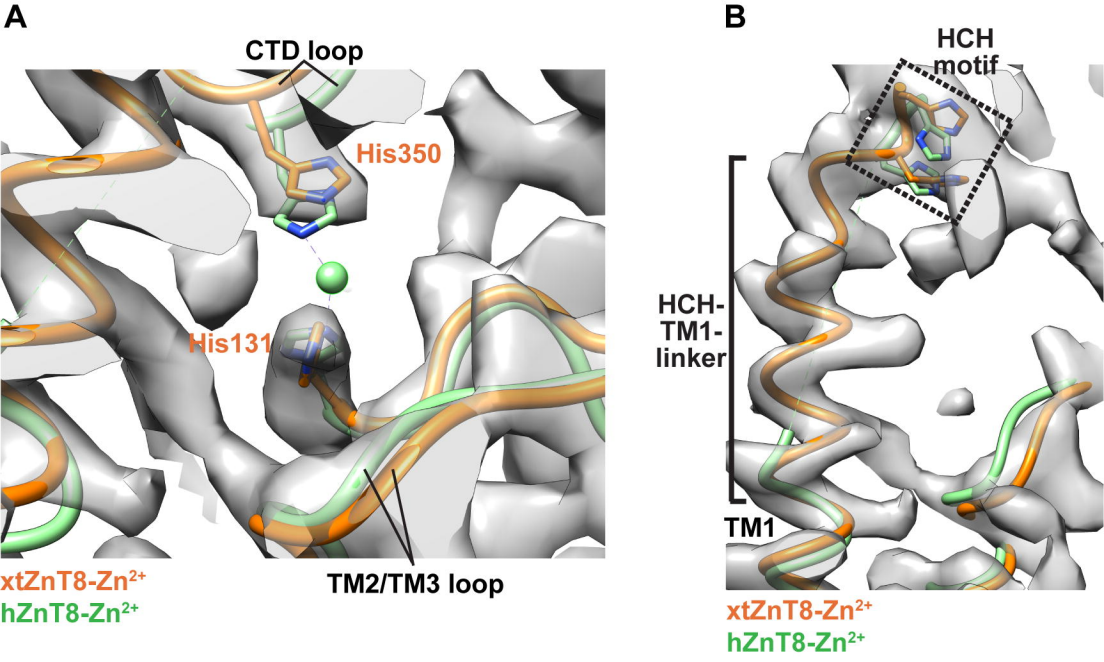
A
CTD loop
His350
His131
TM2/TM3 loop
xtZnT8-Zn2+
hZnT8-Zn2+
B
HCH
motif
HCH-
TM1-
linker
TM1
xtZnT8-Zn2+
hZnT8-Zn2+